LAPPEENRANTA UNIVERSITY OF TECHNOLOGY
LUT School of Energy Systems
LUT Mechanical Engineering

Devika Sasi Ushakumari

PARAMETRIC TOOL FOR INITIAL ESTIMATION OF THERMAL AND MECHANICAL STRESS IN HIGH SPEED ROTORS

Lappeenranta January 19, 2018
Examiners: Professor Jussi Sopanen
Dr. Sc. (Tech.) Rafał Piotr Jastrzębski
Supervisor: M. Sc. (Tech.) Eerik Sikanen

ABSTRACT

Lappeenranta University of Technology
LUT School of Energy Systems
LUT Mechanical Engineering

Devika Sasi Ushakumari

Parametric tool for initial estimation of thermal and mechanical stress in high speed rotors

Master's thesis
2018
86 pages, 26 figures, 37 tables and 4 appendices
Examiners: Professor Jussi Sopanen
Dr. Sc. (Tech.) Rafał Piotr Jastrzebski
Supervisor: M. Sc. (Tech.) Eerik Sikanen

Keywords: Bearingless drive, analytical stress calculation, permanent magnet rotor, high speed rotor, continuous cylindrical permanent magnet, surface permanent magnet, interior permanent magnet, V-shaped magnet.

Bearingless drives magnetically integrate magnetic bearing and motor function. They offer non-contaminating working environment, are maintenance free and generally have long lifetime. Bearingless drives is a good choice in high speed applications due to the absence of friction losses. Permanent magnets employed at the rotor of bearingless drives suffer from mechanical stresses due to high centrifugal forces. Hence, the yield strength of the rotor materials is the only limiting factor of speed in permanent magnet rotors. The stress analysis in permanent magnet rotors are generally carried out using finite element software such as ansys, abaqus etc. This approach is time consuming which limits them in applications where rapid testing of varying geometries is a requirement. Therefore, an analytical tool to predict the initial mechanical stress in high speed permanent magnet rotors is proposed in this thesis. A parametric tool to predict the peak stress for four basic permanent magnet configurations

like cylindrical permanent magnet, surface permanent manet, interior permanent magnet and V-Shaped permanent magnet is developed in matlab 17. The results from matlab code is verified with the help of finite element based software ansys 18. The material properties and geometrical definitions used in the matlab code input is repeated in the ansys model to make a fair comparison of results. Two different test cases like geometry test and speed test were framed to do the testing. The test cases are repeated for all four permanent magnet configurations studied in this paper. Moreover, a correction factor is also introduced in the code from the speed test results to improve the accuracy. The reliability of this factor is ensured by using the same factor for different geometries in geometry test. The analytical tool developed gave faster and moderately accurate results on testing.

ACKNOWLEDGEMENTS

First of all, I would like to thank Professor Jussi Sopanen and Dr. Sc. (Tech.) Rafał Piotr Jastrzębski for the wonderful opportunity they provided me which made this thesis possible. Next, I would like to thank my supervisor Eerik Sikanen for his timely guidance throughout the thesis work. The help and advices provided by my colleagues of LUT machine dynamics laboratory is worth mentioning here. Finally, I extend my gratitude towards my parents and sister who always stood with me with kind encouragement during all the tough times I had to go through during the completion of this thesis work.

Devika Sasi Ushakumari
January 19, 2018

TABLE OF CONTENTS

ABBREVIATIONS AND SYMBOLS

Abbreviations

AC	Alternating current
AMB	Active Magnetic Bearing
CAD	Computer aided design
CSD	Constructive solid geometry
CF	Correction factor
CPM	Cylindrical permanent magnet
CTE	Coefficient of thermal expansion
DVD	Digital Video disk
Dy	Dysprosium
FEA	Finite element analysis
HSPM	High speed permanent magnet
IPM	Interior permanent magnet
L/D	Length to diameter ratio
LHS	Left hand side
Nd	Neodymium
NdFeB	Neodymium iron boron
PM	Permanent magnet
PMB	Passive Magnetic Bearing
rpm	Rotations per minute
SCF	Stress concentration factor
SPM	Surface permanent magnet
VPM	V-shaped permanent magnet

Symbols

α	Coefficient of thermal expansion
A_{eq}	Area of equivalent ring in IPM
A_m	Area of magnet
A_{Fe}	Area of iron bridge

b_m	Breadth of the magnet in IPM and VPM
β	Pole shoe angle in IPM and VPM
∇	Interference fit
ΔT	Thermal gradient
δr	Infinitely small radial distance
$\delta\theta$	Infinitely small angle
E	Elastic modulus
ε_r	Radial strain
ε_t	Tangential strain
h_{eq}	Smallest height of the iron bridge above IPM and VPM
l_m	Length of the magnet in IPM and VPM
P	Contact pressure at the interface of magnet and enclosure
$P_{pre-stress}$	Contact pressure of enclosure against magnet at no load
P_{we}	Reduction in contact pressure at enclosure due to centrifugal forces
P_{wm}	Reduction in contact pressure at magnet due to centrifugal forces
r_{fei}	Inner radius of iron core
r_{feo}	Outer radius of iron core
r_{mi}	Inner radius of magnet in CPM and SPM
r_{mo}	Outer radius of magnet in CPM and SPM
r_{ei}	Inner radius of enclosure in CPM and SPM
r_{eo}	Outer radius of enclosure in CPM and SPM
r_{eqi}	Inner radius of proposed equivalent ring in IPM and VPM
r_{eqo}	Outer radius of proposed equivalent ring in IPM and VPM
r_{cfe}	Centroid radius of iron bridge in IPM
r_{cm}	Centroid radius of magnet in IPM
r_{ceq}	Centroid radius of equivalent ring in IPM
ρ_{eq}	Density of equivalent ring in IPM and VPM
ρ_{fe}	Density of iron bridge in IPM and VPM
ρ_m	Density of magnet in VPM
$\sigma_{pre-stress}$	Enclosure pre-stress before applying rotational load
$\sigma(r_{feo})$	Radial stress at a radius of r_{feo}

σ_r	Radial stress
σ_t	Tangential stress
σ_{teq}	Tangential stress of equivalent ring in IPM
σ_{tmax}	Maximum tangential stress in VPM
θ	Angle between two magnets of a single pole
u	Radial displacement
$u(r_{fei})$	Radial displacement at a radius of r_{fei}
v	Poisson ratio
ω	Angular velocity

1 INTRODUCTION

In recent years, researchers have been increasingly interested in the study of magnetic bearings since smaller drives delivering higher speeds is of great demand in modern industrial applications. Periodical maintenance is challenging in applications such as outer space, drives installed in inaccessible location and hazardous environment where the use of mechanical bearings is irrelevant. Moreover, hygienic standards prevent motor drives with mechanical bearings to be used in industries involving pharmaceuticals, food and beverages and biochemical reactors in order to prevent contamination of products. Furthermore, lubrication oil is not a suitable option in ultra high and low temperature and in high vacuum applications. Magnetically suspending the shaft and rotors eliminate the need of lubrication and frequent maintenance required by mechanical bearings. [1,2]

Magnetic bearings use passive or active magnets to support the shaft radially and axially. Radial magnetic bearing uses an unbalanced radial force produced by difference in magnetic field between radially opposite magnetic poles to suspend the shaft. Axial magnetic bearing or thrust bearing maintains the axial position of the shaft. A rotating shaft can be positioned accurately by five axis magnetic suspension system including two radial units and one axial unit. [3]

Bearingless drives is a good choice in high-speed applications due to the absence of friction, vibration control, and smaller machine footprint. However, electromagnetic design and electromechanical rotor structure optimization are challenging. “Bearingless motor” is a term which originated in the 90s for referring brushless AC (alternating current) motor. The term bearingless evolved over time in the research community. The most appropriate definition for a bearingless motor is given by Chiba as “A magnetic bearing with a magnetically integrated motor function”. Figure 1 shows a twin bearingless drive with 5 axis magnetic suspension. Each bearingless unit incorporates 3 suspension and 3 motor phases. The motor windings in each bearingless unit are series connected and supplied with a 3 phase inverter (3Ø INV) which provides varying voltage and frequency for torque generation. The torque produced by each unit will be half the total torque requirement. Two independent three phase inverters are provided at the suspension windings for producing levitation

current. A single phase inverter (1Ø INV) is provided at the thrust bearing for controlling the axial position of the rotor. [3]

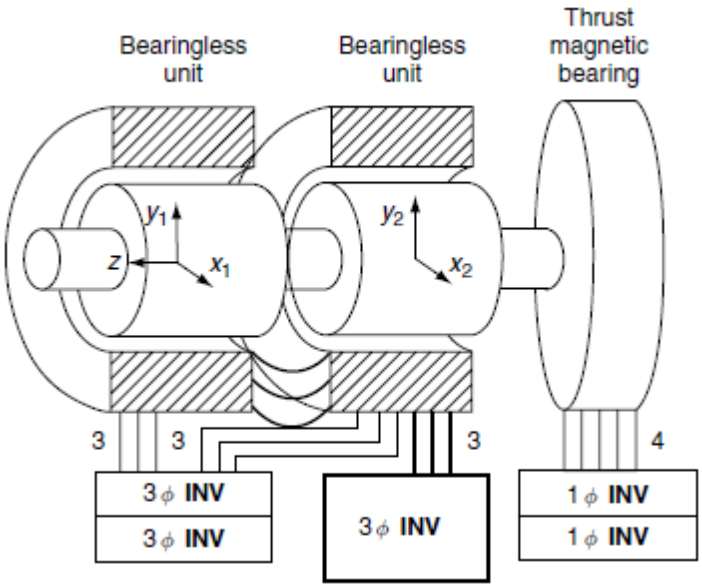

Figure 1. Bearingless drive with 5 axis magnetic suspension. [3]

Bearingless motors are a hybrid of electric motors and magnetic bearings which incorporates an integrated winding system that can generate torque as well as radial forces [4]. The absence of mechanical contact in bearingless drives eliminates friction and wear thereby reducing the maintenance cost and increasing the lifetime [5]. Bearingless motors are either employed as twin bearingless units or come in combination with other bearings such as mechanical or magnetic bearings. Magnetic bearings can be operated either actively as in active magnetic bearings (AMBs) or passively as in passive magnetic bearings (PMBs). Figure 2 shows the combination of bearingless unit with radial magnetic bearing and mechanical bearing. [3]. While AMBs offer the advantage of better control and accurate positioning of shaft, PMBs might provide higher efficiency and lower system complexity. High-speed permanent magnet (HSPM) synchronous motors uses permanent magnets (PM) instead of copper windings eliminating the need of excitation circuit. The absence of copper loss in rotor winding increases the efficiency of the motor and they are capable of maintaining the efficiency even at large variation of the output power. The use of PMs gives this category of machines the highest power density and efficiency. [6]. The major limiting factors while designing a rotor for high speed machine are the centrifugal forces and natural bending frequencies. Centrifugal forces induce mechanical stress, which limits the radius of rotor, and natural bending frequencies sets limitations to the length of the rotor. [7].

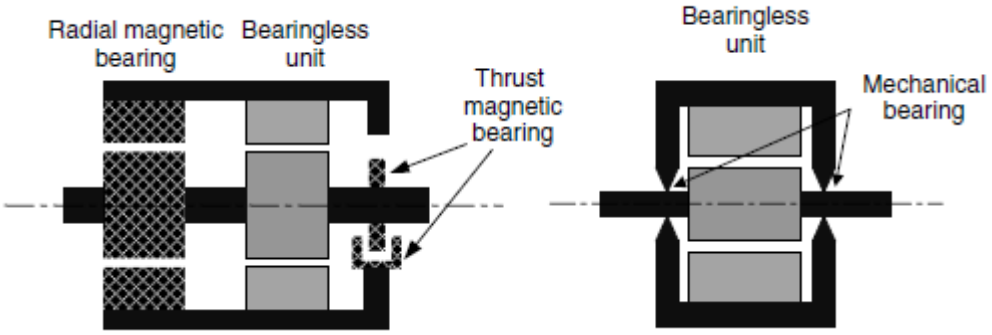

Figure 2. Combination of bearingless unit with radial magnetic bearing (left) and mechanical bearing (right). [3]

1.1 Research Problem

Laboratory of machine dynamics at Lappeenranta University of Technology is currently working on the mechanical design aspects for a project which aims at commercializing the bearingless technology. The two important functions of the proposed bearingless drive are the magnetic levitation of the shaft assembly and providing the shaft with required torque and speed. These two functions have to be optimized in the design of the bearingless drive. The stress analysis in PM rotors are generally carried out using FEM such as Ansys, Abaqus etc. This approach is time consuming which limits them in applications where rapid testing of varying geometries is required. Therefore, an analytical tool to predict the initial mechanical stress in high-speed PM rotors is proposed in this thesis. The objective of the thesis is to develop a parametric tool in Matlab, which predicts the initial mechanical stress in four basic configurations like cylindrical permanent magnet (CPM), surface permanent magnet (SPM), interior permanent magnet (IPM) and V-shaped permanent magnet (VPM). The tool is expected to provide fast and accurate results on initial estimation of mechanical and thermal stress in high speed rotors which can replace the time consuming approach of building a finite element model for every test being performed. It is worth mentioning here that the scope of the developed analytical tool is not limited in predicting the initial stresses in bearingless drives, but it can also be used in other technologies involving PM rotors which are studied in this thesis work. The four PMs studied here are cylindrical permanent magnet (CPM), surface permanent magnet (SPM), interior permanent magnet (IPM) and V-shaped permanent magnet (VPM).

1.2 Limitations

Approximations are inevitable for a study involving analytical calculations which on the other hand diminishes the accuracy of the results obtained. This section of the thesis clearly points out he approximations made and the factors not considered while deducting the results and thereby the conclusion of the thesis work. Firstly, thermal stress are included only in the first model involving a continuous cylindrical structure and in the remaining three models, the effect of thermal analysis is not considered. Moreover, the thermal analysis of the first model does not take into account the thermal gradient existing between different parts of the rotor assembly. Instead a constant temperature difference between the entire rotor assembly and the surroundings is only considered. Furthermore, the coefficient of thermal expansion (CTE) is assumed as a constant. But in reality CTE varies with temperature.

The radial, tangential and von Mises stresses are plotted in Matlab only for CPM. The remaining four models, only the tangential stress is calculated. For IPM and VPM, only the maximum tangential stress is calculated and the developed code does not give information on the stress variation at different regions of the rotor assembly.

The anisotropic behaviour of material like carbon fibre is neglected in this study. Instead, a constant value is assumed for the material properties in Matlab code and the same value is used to build the Ansys model as well.

The transient behaviour of the PM rotor during acceleration and deceleration is not studied in this thesis. The maximum stress occurs with changing momentum instead of steady speed. The stress analysis in this thesis is primarily based on the maximum rotational speed of the rotor.

Fatigue characteristics of the material are neglected in this study because the failure of the rotor is not under the focus of this thesis. The study primarily focus on the initial stress values and the fatigue life analysis does not come under the scope of this thesis work.

The major limitation of this thesis work is the use of an equivalent ring approach in IPM and VPM studies which is adopted due to the complexity in defining mathematical model for these structures in Matlab. This will reduce the accuracy of the stress analysis because the

most probable regions of peak stress like the fillet corners and iron bridges are not accounted in this approach. Therefore, the approach used for IPM and VPM cannot predict the peak stress. The developed Matlab code predicts the maximum tangential stress of the proposed equivalent ring from which the peak stress is calculated by employing a correction factor. Furthermore, the thesis work lacks mathematical formulation to predict the stress concentration factor (SCF) in IPM and VPM rotors. Instead, a correction factor is derived based on the error analysis of studied data. This approach heavily relies on the test conditions used in this thesis and hence cannot be counted as universal.

In VPM structure, the iron core extending outside the magnet is called the bilateral bride and that in between a magnet pair is called the central bridge. These two are the weakest regions in the structure where the peak stress can be expected. But, the peak stress in bilateral bridge appears to be far higher than that at the central bridge. Hence, this thesis does not discuss the peak stress occurring at the central bridge of VPM. Instead the study focuses on finding the maximum stress in VPM which occurs at the bilateral bridge.

1.3 Structure of Thesis

The primary objective of the thesis work is to develop a parametric tool in Matlab which can predict the maximum stress occurring in PM rotors such as CPM, SPM, IPM and VPM due to centrifugal force as a result of high rotational speed. The developed code is used to predict different PM rotors which can be adopted in bearingless technology. The first chapter of this thesis reviews the basic concepts in bearingless technology, defines the objectives of the thesis and outlines the scope or sets out the limitations of the presented thesis. Second chapter studies bearingless drives in detail by comparing them with the other bearing technologies emphasising the relevance of this thesis in the current scenario. The theory behind four different PM rotors are studied in chapter 3 where the works of different authors in similar subject are reviewed. The chapter explains the basic theoretical concepts used to formulate the Matlab tool and lists out all the equations used in the process of developing the tool. The primary step of the adopted methodology for this thesis involves building a tool in Matlab purely based on knowledge from literature review. This tool is then verified against a FE model built in Ansys which is used as the reference source for error analysis. Chapter 4 includes 9 test cases comparing the result of Matlab code and Ansys model built using the same input parameters used by the code. All the four models are tested for three different

geometries and 5 different speeds. In addition, a thermal test is conducted for the CPM which totals to 3 test cases for CPM and 2 test cases for each other model. The error analysis of the Matlab result is also presented in this chapter. The differences between the expected results obtained from FEA and the Matlab results are closely analysed to calculate a correction factor (CF) to improve the results. The calculation of CF and the corrected result are presented in chapter 5. Chapter 6 discuss the possible reason behind the variation of actual result with expected result and comment on the reliability of the approaches adopted on this thesis work. A brief summary of the thesis work is presented in chapter 7 which concludes this thesis. The developed tool in Matlab is presented as appendix.

The thesis is realized in five consecutive phases. In the first phase, the parametric tool is developed in Matlab based on the analytical formulations of four PM rotors studied in literature. The second phase involves building Ansys models for the four PM rotors based on geometry and material properties already defined in Matlab during the first phase. The third phase is the testing phase where Matlab and Ansys results for the same input parameters are compared to find out the error in Matlab code by keeping the corresponding Ansys results as the reference. A correction factor for the analytical tool is calculated in the fourth stage based on the error analysis data from speed test of previous stage. The reliability of this correction factor is tested in the final stage where the CF developed form speed test is used in the geometry test to verify the universal nature of the calculated CF. It is observed that the analytical tool developed gave faster and moderately accurate results on testing.

2 BEARINGLESS DRIVES

Bearingless drives magnetically integrate magnetic bearing and motor function. The term bearingless does not indicate the absence of bearing forces, instead it implies that conventional bearings are absent and the bearing forces are provided by contactless magnetic support [8]. This section first reviews conventional bearings for high speed application and further discusses the basic configurations, speed limits and application areas of bearingless drives.

2.1 Bearing choice for high speed machines

High speed applications provide the advantage of reducing the volume of the electrical machine by compensating the diameter with an increased speed. The bearing choices for a typical high-speed application varies depending on the requirement. Conventional ball bearings are favored for their small size, robustness and low cost. But they have to be lubricated frequently and therefore have a limited lifetime that is dependent on load and speed. In addition, they are quite dependent on the operating temperature that narrow down their application range. [9]

By using fluid film bearings, which can be static or dynamic in nature, we can eliminate the need of lubrication. In case of static bearings, pressure is maintained between the shaft and the journal using an external pump whereas the dynamic bearings are self-starting and do not require external pumping. The lubricating fluid can be air or some other liquid. In case of air bearing, the rotor is levitated by the air pressure generated during the high speed of rotation. The contact between the rotor and journal is lost at high speed eliminating the wear conditions at high speeds ensuring less friction losses and a longer lifetime. Foil bearing is a type of dynamic air bearing which uses spring loaded foil between the shaft and the sleeve. The foil is pushed away from the journal at high speeds thereby eliminating the contact. This bearing can reach up to 70000 rpm. The limitation of these bearings are that, they are only suitable for high speeds, cannot be used for different ranges of speed from low to high and have small air gaps. However, they are very simple and reliable technology that are independent of sophisticated electronics, battery or backup bearings. Because, in case of

power failures, the speed of rotating journal drops down bringing contact between the foil and journal and this mechanism does not require additional safety bearings for support. [9]

In the case of magnetic bearings, where the rotor is levitated using magnetic forces, control system involving sensors and actuators are required for detecting the position of rotor. This makes the technology more complicated than air bearings and also increases the total volume occupied by bearing system. Moreover, magnetic bearings uses backup battery as well as safety precautions to face the situation of power failure. Even then, safety bearings can fail if the journal was rotating at very high speed during the touchdown. Magnetic bearings are favored in applications that require good controllability. [10]. Magnetic bearing offers the advantages of high power density and efficiency [11].

Passive permanent magnet bearings are preferred due to their simple structure, high power density, efficiency, reduced size, lighter structure and small cost. Two basic rotor structures can be made from PMs, integral and block structure. Integral structure constitute solid or hollow cylinder, which offer high mechanical strength while block magnets have a greater utilization rate. Utilization rate of integral structure is not as good as the block structure. The main limitation of block structure is the complexity during manufacturing. [12]

2.2 Basic configurations of bearingless drives

A minimum of two bearingless units are required to accurately position the shaft in radial direction. Each of these bearingless units has six windings in total, 3 for suspension and 3 for torque production. The torque produced in each bearingless unit for a twin bearingless drive will be half of the total torque requirement. In addition a thrust magnetic bearing is also provided in a bearingless drive to control the axial movement of shaft. In total, a bearingless drive has control in 5 axis. Figure 3 shows four variations of twin bearingless drives in clockwise direction. The first variation in clockwise direction correspond to twin bearingless drive with 5 axis position control where rotor assembly rotates inside a stator core. This design is mostly used in applications such as pumps and compressors. The second variation represent a rotor rotating inside the stator and this case mostly occurs in applications such as Digital Video disk (DVD) and hard disk drives. The third variation is a 4 axis bearingless assembly in which the thrust bearing is absent. The two bearingless units are mechanically assembled to maintain axial centering in case of small axial loads. The

fourth variation correspond to 5 axis control of a rotor with hollow shat. This design is mostly applicable in case of flow meters where fluid flow is possible through the center. [3]

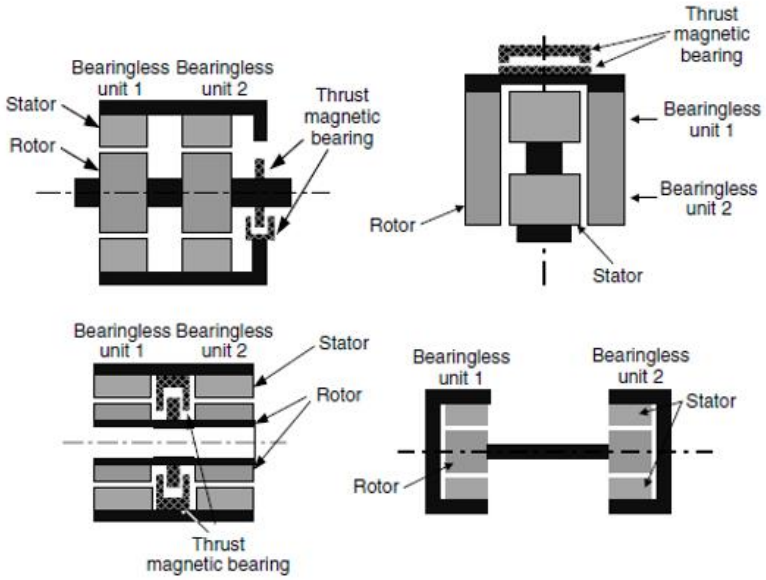

Figure 3. Twin bearingless drives with 5and 4 axis suspension [3]

Magnetic suspension in two axis is possible for specific design as seen in Figure 4. In the first variation, a pivot bearing controls the radial and magnetic position of one end of a vertical shaft. The second variation is a compact design that provides passive axial and radial positioning for a shaftless assembly. [3]

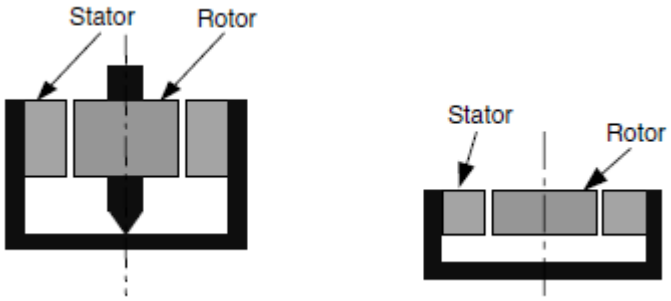

Figure 4. Bearingless drives with 2 axis suspension [3]

2.3 Bearingless drives in high speed applications

Researchers working on bearingless technology has shown great interest in achieving high rotational speed for bearingless drives. A glance at the history of bearingless drive technology shows that there has been a drastic increase in the speed of tested prototype over the years. In early 1990s, the speed of tested prototype ranged from 4000 to 6000 rpm

[13,14]. However, a record speed of 400000 rpm at a surface speed of 146.6 m/s was achieved in 2012 by a group of researchers from ETH Zurich [15].

2.4 Bearingless drives requirements for high speed applications

The major concern of designers while developing bearingless drives for high speed applications is the mechanical stability of rotors. The rare earth magnets used in bearingless rotors have low yield strength and are brittle in nature. It is obvious from test results performed by various researches that an additional bandage is required to support the magnets from high centrifugal forces due to elevated rotational speed. A speed test was conducted by [16] for three different bandage types by keeping all other parameters constant. It is observed that a magnet without a bandage fails at 72000 rpm while that with a carbon fiber bandage was able to withstand 96000 rpm and 0.5 mm hot worked steel bandage crossed a speed limit of 115000 rpm. [1]

Magnetic losses are unavoidable in bearingless drives and they can generally be classified into stator iron losses and rotor eddy current losses. Stator is prone to hysteresis and eddy current loss due to the oscillating magnetic field produced by rotating rotor. Hysteresis loss can be minimized by using a magnetic material which has high relative permeability and low coercive field strength. High electrical resistivity of the stator material further limits the eddy current loss. Eddy current loss is common in rotors especially if they are provided with electrically conducting bandage or if the stator is slotted. The most common practice of laminating the rotor reduces the mechanical strength. The optimum solution is to avoid a slotted stator. The use of sinusoidal current control instead of square wave current control can further reduce the rotor eddy current loss. [16]

The most common choice for magnetic material for high speed application are alnico magnets, ferrite magnets and rare earth magnets. Rare earth magnets possess the property of high residual magnetic flux density and coercive force. [12]. Rare earth magnets can either be made of light rare earth material like Neodymium (Nd) or heavy rare earth material like dysprosium (Dy). Dysprosium improves the magnetic coercivity due to which the magnet will be able to retain the magnetic properties at elevated temperature. [17].

The two common material choice for rotor enclosure are titanium alloy and carbon fiber or epoxy glass. Light weighing carbon fiber has the advantages of good strength to weight ratio and low electrical conductivity which in turn reduces the heat generation due to eddy current. However, carbon fiber has poor thermal conductivity making the cooling process of magnet more difficult. Titanium alloys have good tensile strength and better thermal conductivity enabling rapid cooling of magnets. The major limitation in using Titanium alloy is its high electrical conductivity due to which the heat loss due to eddy current flow is high.[12]

2.5 Bearingless drives applications

The most obvious application area of bearingless drive are for pumps and compressors that are required to work in contamination free environment where lubrication and corrosion effects from mechanical bearings are unacceptable. This led many researchers to focus the study of bearingless motors to drive pumps used in artificial hearts and blood pumping system where even minor contamination leads to most dangerous consequences.

A bearingless disk motor is proposed in [18] for centrifugal blood pump in artificial hearts which uses a C-shaped stator core to make the design thin and compact. The bearingless drive in this application prevents blood damage and contamination and makes the implantation possible in less space. Meanwhile Yang and Sheng in [19] comments on the requirement of complex hardware and control system in bearingless motors in which 2 sets of windings needs to be controlled and synchronized. The authors again propose a magnetic suspension which uses two passive magnetic bearings in radial direction and employs an electromagnetic actuator in the axial direction to solve this problem. An alternate solution to the complexity of separate torque and levitation windings is to couple both the windings into a combined winding system. A comparison study of separate windings and combined winding system is made by [20] who concludes that for high power input both the windings achieve comparable speed whereas in the case of low power output, the speed is reduced considerably in combined winding system. Meanwhile, [21] developed a centrifugal blood pump of 3.5 W power rating and 5 l/min flowrate which is levitated and rotated by a bearingless rotor.

The agitator in bioreactors as well as pharmaceutical mixers require high purity mixing conditions. The application of magnetic bearings in these areas are studied in [22] and [23].

In addition to the leakages and corrosion debris from mechanical bearings, the shear force developed at the gap of these bearings can damage and contaminate the delicate liquids used in pharmaceutical applications. It is a necessity to maintain the cell structure when biological fluids are processed. This demand led [23] to develop a bearingless motor for pharmaceutical mixing in which an exterior rotor is suspended and rotated by bearingless motor. A hygienic and cell friendly environment is required in order to culture cells and perform biological reactions in a bioreactor. And hence the agitator equipped for this application needs to be supported by a contamination free bearing which is proposed by [22].

3 STRESS ANALYSIS OF ROTATING CYLINDERS AND BASIC MAGNET CONFIGURATIONS

The basic theory of rotating cylinders under centrifugal load is reviewed in this chapter, followed by the application of the theory to find out the maximum stress for the four different types of PM rotors. Initially, the equations of radial and tangential stress are derived by considering an infinitely small rotating ring element. These equations are consequently used to find the radial and tangential stress in CPM by applying boundary conditions of three shrink fitted tubes to the derived equations. The same principle is applied for SPM as well. In case of IPM, an equivalent ring is considered such that the mass density of the proposed ring is equivalent to the combined mass density of the magnet and iron bridge above and on both sides of the magnet. A similar approach is used in VPM to transfer the mass density to equivalent ring, but centroid radius of all the constituting regions are taken into account instead of average radius.

In order to derive the radial and tangential stress acting on a rotating solid cylinder, an infinitely small portion of the cylinder is considered which is located at a distance of r from the center. The section has a radial length of δr, axial length of unity and makes an angle of $\delta\theta$ at the center of cylinder. Figure 5 depicts the free body diagram of the element due to stress created under centrifugal forces. It is observed that horizontal component of forces ($\sigma_t \delta r. 1 \cos\frac{\delta\theta}{2}$) on the both sides of the element cancel out each other due to the symmetry. The vertical components are equated to the centrifugal force to express the equilibrium condition. [24]

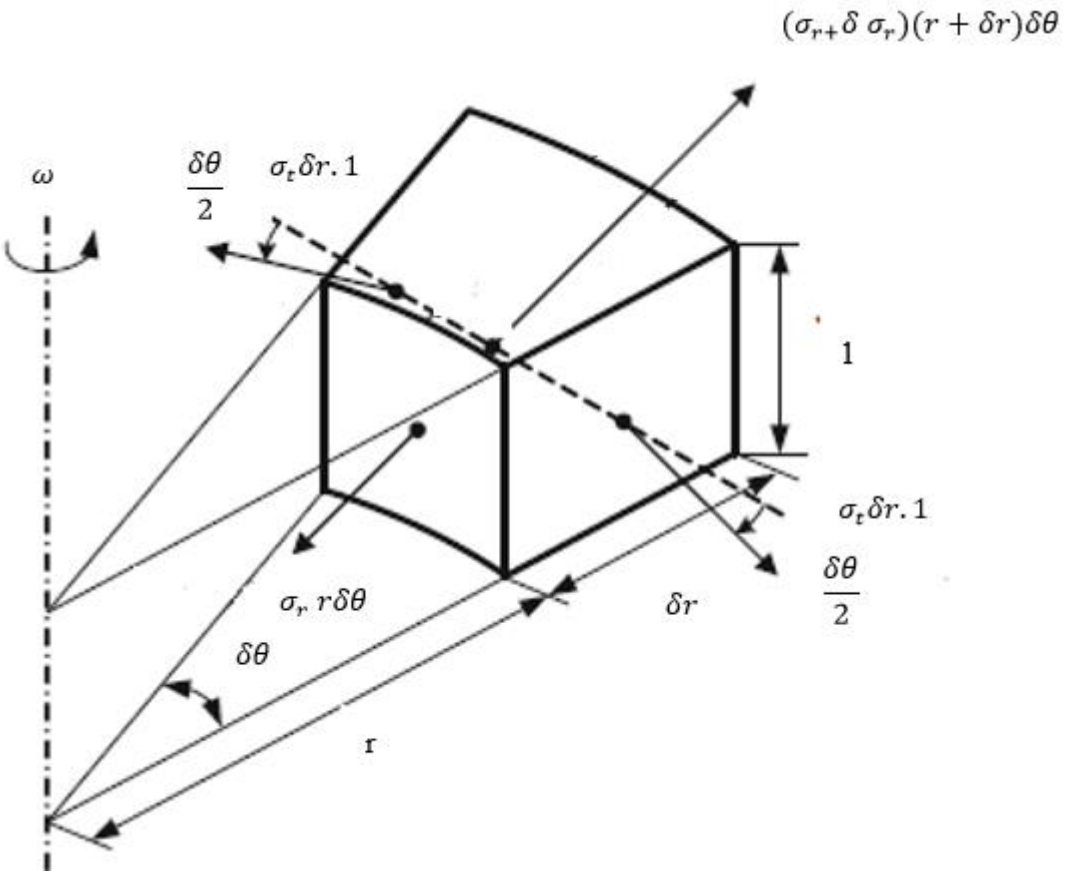

Figure 5. Free body diagram of an infinitely small element of a solid cylinder under centrifugal forces [9]

From Figure 5, the centrifugal force can be derived as given below.

The volume of element = $r\delta\theta\delta r.1$

Mass of the element = $\rho r\delta\theta\delta r$

Centrifugal force = $m\,\omega^2 r = \rho r^2 \omega^{\,2}\delta\theta\delta r$

Where ρ and m are the density of the material and mass of the ring respectively. The area of different planes of the section is first calculated in order to convert radial and tangential stress to corresponding forces in equilibrium equation.

Area of tangential plane of the element at right and left = $\delta r.1$

Area of lower radial plane of the element = $r\delta\theta.1$

Area of upper radial plane of the element = $(r+\delta r)\delta\theta.1$

The equilibrium condition is expressed as below

$$2\sigma_t \delta r \sin\frac{\delta\theta}{2} + \sigma_r\, r\delta\theta - (\sigma_r + \delta\sigma_r)(\, r + \delta r)\delta\theta = \rho r^2 \omega^{\,2}\delta\theta\delta r \qquad (1)$$

The above equation is further expanded after approximating the small angle $\sin\frac{\delta\theta}{2}$ as $\frac{\delta\theta}{2}$ radian.

$$2\sigma_t \frac{\delta\theta}{2}\delta r + \sigma_r\, r\delta\theta - \sigma_r\, r\delta\theta - \sigma_r\, \delta r\delta\theta - \delta\sigma_r\, r\delta\theta = \rho r^2 \omega^{\,2}\delta\theta\delta r \qquad (2)$$

$$\frac{2\sigma_t \frac{\delta\theta}{2}\delta r - \sigma_r\, \delta r\delta\theta - \delta\sigma_r\, r\delta\theta}{\delta\theta\delta r} = \rho r^2 \omega^{\,2} \qquad (3)$$

Applying the limit as $\delta r \rightarrow 0$, $\delta\sigma_r \rightarrow 0$ in the above equation further reduces the terms to

$$\sigma_t - \sigma_r - r\frac{\partial\sigma_r}{\partial r} = \rho r^2 \omega^{\,2} \qquad (4)$$

As the cylinder rotates, there is a radial movement in the element which is denoted as u. The radial strain is the rate of change of the radial shift with respect to the radius as given below.

$$\varepsilon_r = \frac{\delta u_r}{\delta r} = \frac{\sigma_r - \nu\sigma_t}{E} \qquad (5)$$

The diametrical strain is equal to the tangential strain according to the author referred in [24]

$$\frac{u_r}{r} = \left(\frac{\sigma_t - \nu\sigma_r}{E}\right) \qquad (6)$$

Which implies

$$u_r = r\left(\frac{\sigma_t - \nu\sigma_r}{E}\right)$$

Differentiating with respect to radius r implies

$$\frac{\partial u_r}{\partial r} = \frac{1}{E}\left[(\sigma_t - \nu\sigma_r) + r\left(\frac{\partial\sigma_t}{\partial r} - r\,\frac{\partial\sigma_t}{\partial r}\right)\right] \qquad (7)$$

Equating equations (5) and (7) gives the relation

$$(\sigma_t - \sigma_r)(1+\nu) + r\frac{\partial \sigma_t}{\partial r} - r\nu\frac{\partial \sigma_r}{\partial r} = 0 \tag{8}$$

Substituting $(\sigma_t - \sigma_r)$ from (4) implies

$$\left(r\frac{\partial \sigma_r}{\partial r} + \rho r^2 \omega^2\right)(1+\nu) + r\frac{\partial \sigma_t}{\partial r} - r\nu\frac{\partial \sigma_r}{\partial r} = 0 \tag{9}$$

$$\frac{\partial \sigma_t}{\partial r} + \frac{\partial \sigma_r}{\partial r} = -\rho r^2 \omega^2 (1+\nu) \tag{10}$$

Integrating the above relation gives

$$\sigma_t + \sigma_r = -\rho r^2 \omega^2 (1+\nu) + 2a \tag{11}$$

Where 2a is the constant of integration

Subtracting (4) from above relation gives

$$2\sigma_t + r\frac{\partial \sigma_t}{\partial r} = -\frac{\rho r^2 \omega^2}{2}(3+\nu) + 2a \tag{12}$$

But the LHS of above relation can also be expressed as below

$$2\sigma_t + r\frac{\partial \sigma_t}{\partial r} = \frac{\partial (r^2 \sigma_r)}{\partial r}\frac{1}{r} \tag{13}$$

Substituting the LHS by the alternative expression gives the below relation

$$\frac{\partial (r^2 \sigma_r)}{\partial r} = r\left[-\frac{\rho r^2 \omega^2}{2}(3+\nu) + 2a\right] \tag{14}$$

Integrating the above relation gives

$$r^2 \sigma_r = -\frac{\rho r^4 \omega^2}{8}(3+\nu) + \frac{2ar^2}{2} - b \tag{15}$$

Where *b* is the second integration constant

$$\sigma_r = a - \frac{b}{r^2} - (3+\nu)\frac{\rho r^2 \omega^2}{8} \tag{16}$$

From equation (8) and (16), we can find the tangential stress as given below.

$$\sigma_t = a + \frac{b}{r^2} - (1+3\nu)\frac{\rho r^2 \omega^2}{8} \tag{17}$$

Equations (16) and (17) gives the general equations for radial and tangential stress in a rotating cylinder subjected to centrifugal forces.

Alternatively, Larsonneur uses a similar approach in which any point in the element of an axisymmetric ring is assumed to move only in radial direction. The radial displacement is taken as a function of radius which is derived in three steps. In the first step, radial and tangential strain are expressed in terms of radial displacement. Next, differential equation for radial displacement is derived by combining the equilibrium equations of ring and the strain equations using Hooke's law. Finally, the differential equation is solved to get a generalized equation for radial displacement. The general equation of displacement has two integration constants which can be solved by applying boundary conditions to the specific geometry under consideration. Radial and tangential stress can be solved subsequently from displacement equation. [25]

In general, strain can be defined as the change in length of a specific component per unit length of the component when a force is acting in the direction of deformation. The strain in radial and tangential directions denoted by ε_r and ε_t can be derived as below.

$$\varepsilon_r = \lim_{dr \to 0} \frac{u(r+dr) - u(r)}{dr} = \frac{\delta u_r}{\delta r} \tag{18}$$

$$\varepsilon_t = \frac{\lim_{\delta\theta \to 0} \Big(\big(r + u(r)\big)\delta\theta - r\delta\theta \Big)}{r\delta\theta} = \frac{u_r}{r} \tag{19}$$

The equilibrium equation is derived and simplified using the same approach followed in the previous section and hence equations (1) and (4) can be referred here.

$$r\frac{\delta\sigma_r}{\delta r} = \sigma_t - \sigma_r - \rho r^2 \omega^2 \tag{20}$$

The Hooke's law can be simplified to form the equations (21) and (22) for radial and tangential strain respectively.

$$\varepsilon_r = \frac{\sigma_r - \nu\sigma_t}{E} \tag{21}$$

$$\varepsilon_t = \frac{\sigma_t - \nu\sigma_r}{E} \tag{22}$$

Where ν and E denotes the poisson ratio and elastic modulus of the material respectively. Finally by solving the equations from (18) to (22), a simple differential equation for the displacement 'u' can be derived as below.

$$\frac{E}{1-\nu^2}\left(r^2\frac{\partial^2 u}{\partial r^2}+r\frac{\partial u}{\partial r}-u\right)=-\rho r^3\omega^2 \tag{23}$$

General solution for the differential equation (23) can be represented as given below in equation (24) which is the displacement equation.

$$u(r)=ar+\frac{b}{r}-\frac{1-\nu^2}{8E}\rho r^3\omega^2 \tag{24}$$

Where a and b are the integration constants. Integration constants can be found by applying boundary conditions to the specific scenario. For n number of shrink fitted components, 2n boundary conditions can be obtained and hence a set of 2n equations can be formed. Equations (18),(19),(21),(22) and (24) can be solved simultaneously to find radial and tangential stress and radial displacement.

3.1 Continuous Cylindrical Permanent Magnet

The simplest form of PM rotor is an integral structure involving a hollow cylindrical magnet shrink fitted to the iron core. An enclosure made of carbon fiber or non-magnetic alloy is shrink fitted to the magnet which aids the magnet against failure under centrifugal forces. The shaft is generally made of steel and the permanent magnet is made of a ferromagnetic material. The three parts are assembled as shown in Figure 6.

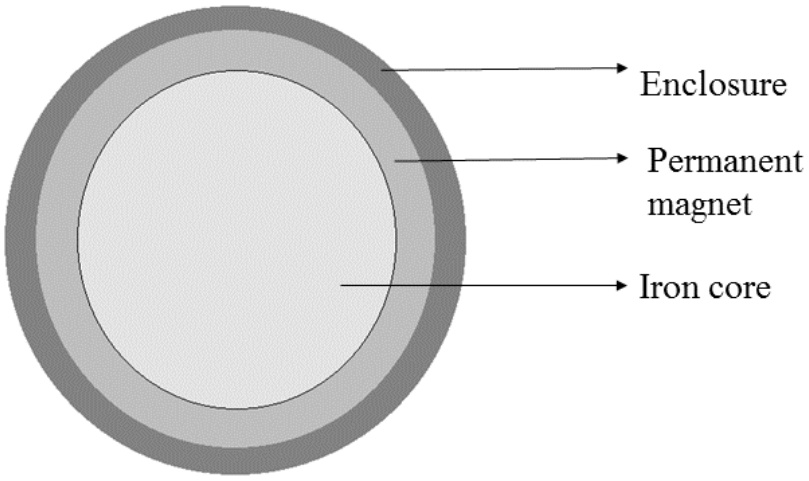

Figure 6. Continuous cylindrical permanent magnet showing the three shrink fitted components

Due to the high speed in rotation of rotor, there will be centrifugal forces acting on it whose magnitude is proportional to the material the rotor is made of, its geometry and shape as well as the speed of rotation. Radial and tangential stress will be induced in each rotating layer of

the rotor. In addition, interference pressure exists in the interface of two shrink fitted structures which is equal to the contact pressure at the interface. In order to calculate the radial and tangential stress, which varies continuously from the centre of rotation to the outermost layer of the outer ring, we use the systematic approach followed by Larsonneur discussed previously. [25]

In order to derive the equations used for stress calculation, the following assumptions are considered [25].

1. The rotor material is homogenous and isotropic.
2. The rotor geometry is axisymmetric.
3. Length of the rotor is short and the rotor is free to expand in axial direction due to which there is no axial stress acting on the rotor. Therefore, the concepts of planar stress and strain can be considered.
4. Shear stress acting on the surface is zero due to symmetry of rotor.

In this study we are considering 3 shrink fitted components giving n a value of 3. Therefore, we can obtain 2n=6 boundary conditions and correspondingly 6 equations to solve 6 integration constants.

The boundary conditions are derived based on the following criterion.

1. For a solid shaft, the displacement at center cannot be infinite and for a hollow shaft, stress at inner radius is zero since it is free to expand.
2. The total sum of radius and radial displacement will be equal for two adjacent layers.
3. Stress at the outer radius of the outermost component will be zero since it is free to expand.

Boundary conditions for n=3 is listed below as equation set (25)

$$\begin{cases} u(r_{fei}) \neq \infty \\ \sigma(r_{feo}) = \sigma(r_{mi}) \\ r_{feo} + u(r_{feo}) = r_{mi} + u(r_{mi}) \\ \sigma(r_{mo}) = \sigma(r_{mi}) \\ r_{mo} + u(r_{mo}) = r_{ei} + u(r_{ei}) \\ \sigma(r_{eo}) = 0 \end{cases} \tag{25}$$

Where r_{fei} and r_{feo} refers to the inside and outside radius respectively of the iron core. Similarly, r_{mi} *and* r_{mo} corresponds to that of magnet and r_{ei} and r_{eo} refers to that of enclosure.

Boundary conditions listed in (25) can be solved to get the integration constants a and b in the equation (24) for all the three shrink fitted components. The displacement equation is differentiated with respect to the radius to get the radial strain equation as given in equation (26). It is then combined with the radial strain equation of Hooke's law to obtain the radial stress as given below in equation(27).

$$\varepsilon_r = a - \frac{b}{r^2} - \frac{(3(1-v^2)\rho r^2\omega^2)}{8E} \tag{26}$$

$$\sigma_r = \frac{E(\varepsilon_r + v\varepsilon_t)}{(1-v^2)} \tag{27}$$

Similarly, the displacement equation is divided by the radius to get the tangential strain as given in equation(28). It is then combined with the tangential strain equation from the Hooke's law to get the tangential stress equation as given in equation(29).

$$\varepsilon_t = a + \frac{b}{r^2} - \frac{\left((1-v^2)\rho r^2\omega^2\right)}{8E} \tag{28}$$

$$\sigma_t = \frac{E(\varepsilon_t + v\sigma_r)}{(1-v^2)} \tag{29}$$

Chen and Zhu studied the stress in the PM and enclosure in [12] where the thermal gradient is also taken into account. In this approach, the contact pressure at the interface of magnet and enclosure is initially assumed as P. The analytical equations for stress and displacement is formulated using the differential equation of PM and enclosure. The equations for radial displacement, radial and tangential strain, radial and tangential stress are given by equations (30) to (34) respectively. The effect of temperature rise is accounted while writing the strain equations. Boundary conditions involving the contact pressure is used to solve the integration constants. Finally, the contact pressure is found using the relationship between radial displacement of PM and enclosure at the contact surface.[12]

$$u(r) = ar + \frac{b}{r} - \frac{1-v^2}{8E}\rho r^3\omega^2 + \alpha(1+v)\frac{1}{r}\int_{ri}^{r}\Delta T r dr \tag{30}$$

$$\varepsilon_r = \left(\frac{\sigma_r - \nu\sigma_t}{E}\right) + \alpha\Delta T \tag{31}$$

$$\varepsilon_t = \left(\frac{\sigma_t - \nu\sigma_r}{E}\right) + \alpha\Delta T \tag{32}$$

$$\sigma_r = \frac{E(\varepsilon_r + v\varepsilon_t - \alpha(1+v)\Delta T)}{(1-v^2)} \quad (33)$$

$$\sigma_t = \frac{E(\varepsilon_t + v\sigma_r - \alpha(1+v)\Delta T)}{(1-v^2)} \quad (34)$$

Where α represent the material constant representing the rate of thermal expansion, ΔT is the temperature rise in the material, v is the Poissons ratio

The boundary conditions in rotor enclosure and PMs are given by equations(35), (36) and (37) respectively. The relationship between radial displacement of PM and enclosure at the contact surface is used to solve the contact pressure which is given in equation(38). [12]

$$\sigma_{rei} = -P \quad (35)$$

$$\sigma_{reo} = 0 \quad (36)$$

$$\sigma_{rmo} = -P \quad (37)$$

$$U_{rei} - U_{rmo} = \nabla \quad (38)$$

Where $\sigma_{rei}, \sigma_{reo}$ and σ_{rmo} represent the radial stress at inner surface of enclosure, at the outer surface of enclosure and at the outer surface of PM respectively. U_{rei} and U_{rmo} denotes the radial displacement at inner surface of enclosure and the outer surface of permanent magnet respectively. ∇ denotes the interference fit between manet and enclosure.

The stress analysis by Chen and Zhu concludes that the radial stress in the PM reduces along the radial direction outward and the stress is always negative or compressive in nature. The negative stress at the interface of magnet and enclosure makes sure that the contact is not lost at high surface velocities. The tangential stress in the magnet also decreases radially outward which is also compressive in nature. The von Mises stress, being a root mean square value increases radially. The static stress which is generated when the rotor is at rest due to the interference fit is a constant value throughout the radius and is compressive in nature. The compressive stress in the magnet reduce further with rise in temperature. [12]

The stress analysis in the rotor enclosure done by Chen and Zhu further shows that the radial stress increases radially from a negative value and approaches zero at the outermost layer.

The compressive stress reduces slightly during rotation when compared to the static state because the centrifugal forces produce tensile stress, which will make the compressive stress less influential during rotation. Temperature rise will further reduce the radial stress. Meanwhile, the tangential stress and the von Mises stress decreases radially from a positive value. Rise in temperature further reduces the tensile tangential stress. [12]

3.2 Surface Permanent Magnet

Permanent magnets are mounted on the surface of the rotor in various configurations, which are classified together as Surface Permanent Magnet (SPM) rotors. The magnets are arranged generally as a pair of 2, 4 or that of higher order. The gap between the poles are either left empty or filled using a filler material. The filler choices are carbon fiber, plastics or non-magnetic metals such as titanium alloy. The magnets in one pole can further be segmented to smaller division. However, the segmentation has little effect on reducing the stress level in the enclosure.[26]. Figure 7 shows a four pole SPM.

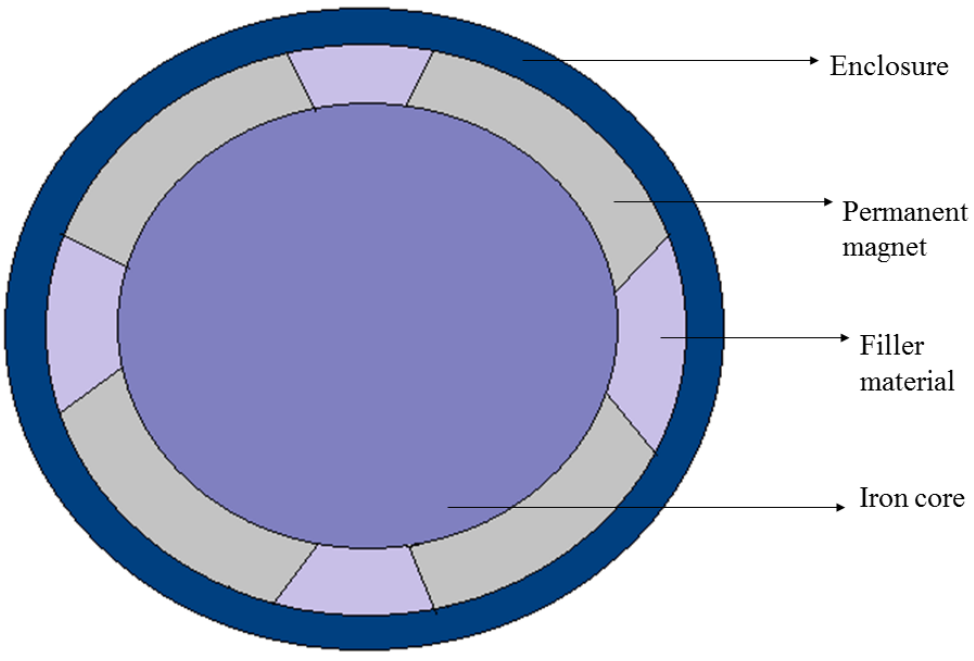

Figure 7. Surface permanent magnet structure

The filler materials are used to prevent the rotor enclosure from bending at the magnet edges and for the safe pressing of enclosure into the magnet. Filler materials also reduce the radial and tangential stress in the rotor enclosure significantly. Maximum tangential stress occurs

in the enclosure at the pole gap region. Radial stress between the rotor core and PM increase with the addition of plastic filler material due to the high thermal expansion coefficient of plastic. However, the tangential stress in the PM varies very little with the addition of filler material. Plastic filler materials possess relatively low stiffness resulting in greater yielding which in turn leads to the highest radial and tangential stress in enclosure as well as the highest radial stress in the magnet. Carbon fiber filler produce intermediate stress level and metal alloy filler produce the lowest stress. However, carbon fiber has its limitation of high cost and difficulty in assembly, while metal alloy limits its usability due to eddy current losses.[26]

While the PMs are glued to the surface of rotor structure, an interference fit is used to join the magnets and the enclosure. Interference fit increases the tangential stress which is more predominant in the enclosure and reduces the tangential stress in the PM. Increasing the enclosure thickness will reduce the stress levels at the cost of higher heat dissipation losses since the increased thickness requires more permanent magnets to generate the necessary air gap flux density. Hence, a balance in the thickness and interference is required for optimizing the stress level. Zhang and Fengge studied rotor retaining sleeve design in [26] and found that stresses are minimal at 0.2 mm interference fit and 10 mm enclosure thickness.[26]. The pre-stress achieved by the interference fit when rotor is at rest is close to the total stress in the enclosure at its operating speed. But, it is never equal since the rotor expands slightly at high speed releasing some stress and hence compressive stress decreases. Consequently, the total stress increases by a small amount from the pre-stress applied. Erik and Bulent has proposed a formula to calculate the desired pre-stress required to prevent loss of contact, which is presented below in equations (39) and (40).[27]

$$\sigma_{pre-stress} = \frac{P_{pre-stress} r}{t_s} \tag{39}$$

$$P_{pre-stress} = (P_{wm} + P_{we})1.2 \tag{40}$$

$\sigma_{pre-stress}$ gives the enclosure pre-stress before applying rotational load for a rotor radius of r where $P_{pre-stress}$ is the contact pressure of enclosure against magnet and P_{wm} & P_{we} represents the amount of reduction in contact pressure at magnet and enclosure respectively due to the rotational velocity.

Temperature and rotational velocity are the major factors deciding the stress levels in a rotor structure. The tangential stress in PM increases with increase in velocity as well as with temperature. Meanwhile, the tangential stress in enclosure increase considerably with an increased temperature. However, it shows only small change with a change in velocity.[26]

Zhang et.al proposes a hybrid structure involving a retaining sleeve with 1 mm thick titanium alloy enclosed by a 6 mm thick carbon fiber layer. This structure reduces the high bending stress and edge stress generated while using the enclosure made from carbon fiber alone. The tangential stress in the enclosure structure reduce by 100 MPa while the radial and tangential stress in the permanent magnet increase by 5 MPa.[26]

While enclosure stress and rise in temperature primarily determines the maximum attainable velocity of the rotor and consequently the design radius, the length of the rotor is determined by the natural bending frequencies. Although the design aspects like the optimum radius, velocity and length of the rotor is not considered in this thesis, literature review has shown that the enclosure stress reduces sharply with an increase in L/D (length to diameter) ratio up to a value of 2 and after which the graph approaches a constant trend with only a slight reduction in stress when the impact of enclosure stress is studied at constant values of power rating and rpm. [27]

SPM is analogous to CPM when a section including the rotor core, magnet and enclosure is considered. Hence, equations (18),(19),(21),(22) and (24) can be reused here as well to find the maximum tangential stress above the magnet. The basic difference between CPM and SPM is that magnets are not shrink fitted but instead they are glued to the rotor core. The major drawback of using this approach to calculate the maximum tangential stress is that, the solution is not able to predict the peak stress which occur in the enclosure above the filler material. This is because, the boundary conditions are derived based on interactions in radial directions and hence the contact between filler material and magnets in tangential direction is not accounted. The absence of boundary conditions at the contact surface of PM and filler makes it difficult to predict the peak stress.

3.3 Interior Permanent Magnet

Permanent magnets are buried in rectangular or circular slots inside the iron core of the rotor in the Interior Permanent Magnet (IPM) structure. This structure is more robust in comparison with SPM and hence it does not require enclosure made of carbon or glass fiber which will reduce the equivalent air gap length. Flat or rectangular magnets are much cheaper and hence more popular than circular magnets. The maximum von Mises stress in the rotor structure is greatly dependent on the shape of the magnet slot edge. Therefore, providing a circular fillet with bigger radius will considerably reduce the peak stress. The major limitation in IPM structure is the flux leakage due to iron surface brace. [28,29]

In practical applications, a small tolerance in dimension is maintained at the magnet and magnet slot connection. Magnets are inserted and bonded with an adhesive whose strength is time dependent. Therefore, studying the bonded surface connection between magnet and slot is not sufficient and hence frictional surface is tested in Ansys model in this thesis. The two characteristics which are not accounted in this study of IPM structure are the momentum of rotor during acceleration and deceleration and the fatigue analysis of rotor material. [30]

The most important feature to be considered while designing an IPM rotor is the rotor bridge which is the rotor extending outside the magnet pole. This region is of great interest in electromagnetic as well as mechanical design aspects. The thinner the bridge, the better the electromagnetic performance due to reduced flux leakage. Whereas mechanical performance is compromised at thinner bridges since centrifugal forces are more prominent in these regions. [30] Since electromagnetic aspects are not given much importance in this thesis, a simple semicircular magnet slot ends and a 2 mm thick rotor bridge is considered in this study.

Due to the complexity in calculating the stress in this structure analytically, an equivalent structure is proposed by [29]. Figure 8 shows the comparison of real and proposed equivalent structure.

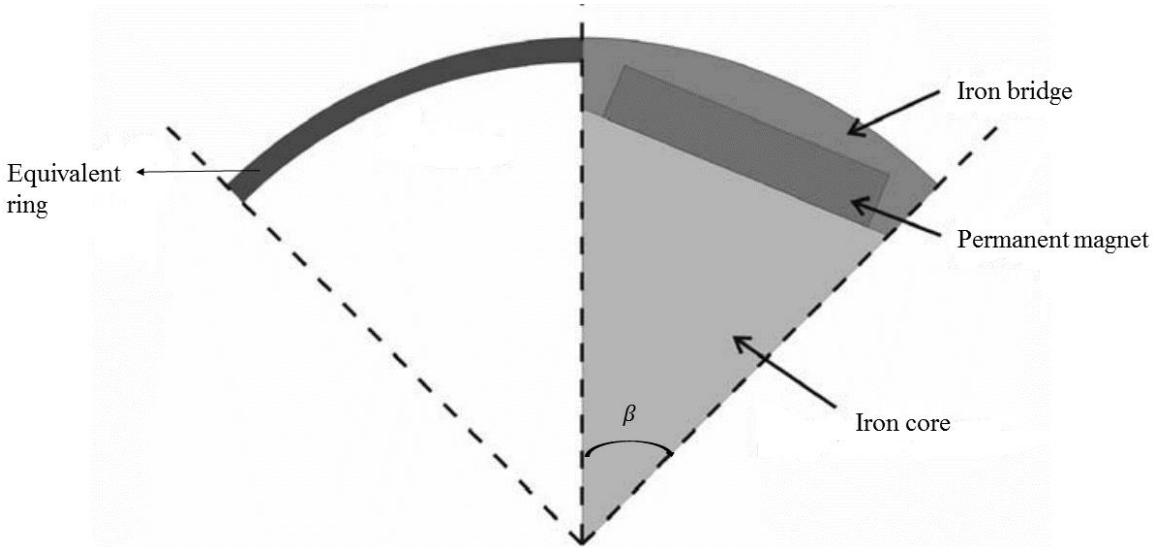

Figure 8. Comparison of real (right) and proposed equivalent structure (left) [29].

In this approach, the centrifugal forces acting on the iron bridge and the magnet is transferred to an equivalent ring. The mass density of magnet as well as that of iron core is used to calculate the equivalent mass density of the ring ensuring that the equivalent ring experience the same centrifugal force as that of the original rotor structure. The height of the equivalent ring h_{eq} is chosen according to the smallest height of the iron bridge above the magnet. The equivalent height can provide the inner and outer radius r_{eqi} and r_{eqo} of the ring. The area of the equivalent ring (A_{eq}) is calculated from both the radius and the angle β, which is the angle included by the magnet as seen from Figure 8. Area of the magnet (A_m) is calculated using the length and breadth of the magnet given by l_m and b_m respectively. Finally, the equivalent mass density of ring (ρ_{eq}) is calculated using mass density of iron core (ρ_{fe}), the area of magnet, area of iron bridge (A_{Fe}) and equivalent area of ring as given in equation (41). [29] [31]

$$\begin{Bmatrix} r_{eqi} = r_{feo} - h_{eq} \\ r_{eqo} = r_{feo} \\ A_{eq} = \dfrac{\beta\left({r_{eqo}}^2 - {r_{eqi}}^2\right)}{2} \\ A_m = l_m b_m \\ A_{fe} = \left(\dfrac{\beta.\left({r_{eqo}}^2 - \left(r_{eqi} - b_m\right)^2\right)}{2}\right) - A_m \\ \rho_{eq} = \rho_{fe}\dfrac{(A_m + A_{Fe})}{A_{eq}} \end{Bmatrix} \quad (41)$$

Where r_{feo} denotes the outer radius of iron core. The tangential stress experienced by the equivalent ring (σ_{teq}) is calculated using the equation(42).

$$\sigma_{teq} = (\frac{r_{eqi} + r_{eqo}}{2})^2 \omega^2 \rho_{eq} \quad (42)$$

There are three different possibilities of error in the above mentioned method. Most importantly, this relationship does not take into account the peak stress occurring at the corners of magnet slots. Moreover, there are small approximations in the calculation of area of iron bridge. Finally, the calculation of equivalent density based on equivalent area is a naive approach. Hence, the below method is proposed where the centroid of different regions is also taken into account to get better accuracy while studying varying geometries.

First of all, a rotor section of angle β is considered which embeds a single magnet pole. Angle β can be varied to study different magnetic pole configurations, for example, β=90 degree correspond to a four pole rotor configuration. Four regions are considered to calculate the density of the equivalent ring region. The first region represents the total area of the rotor core including the magnet which is subtitled as '1'. The second region corresponds to the iron bridge above and on the sides of the magnet pole which is denoted by the subtitle '2'. The third region correspond to the magnet and is denoted by subtitle '3'. The fourth region under consideration is the area below the inner diameter of equivalent ring denoted by the subtitle '4'.

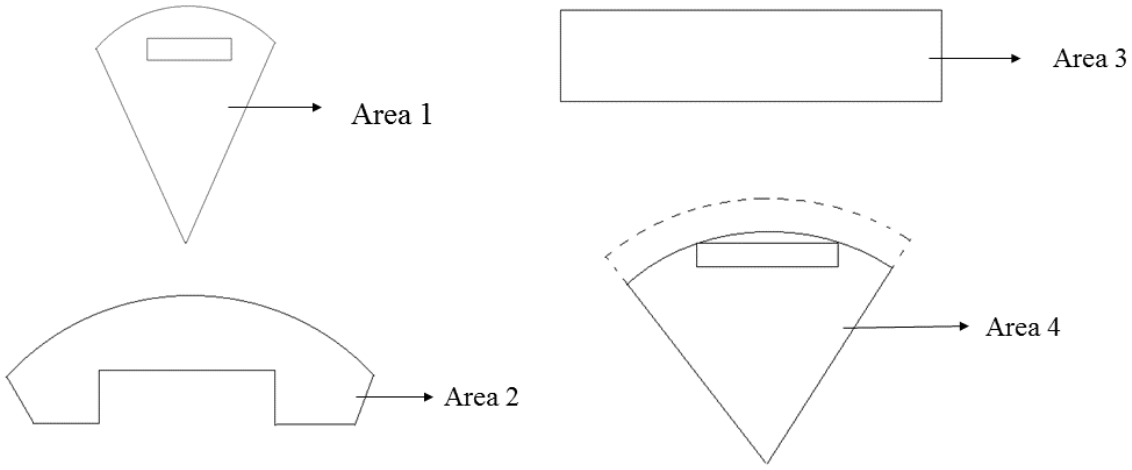

Figure 9. The four different regions of an IPM considered to calculate the equivalent density

The centroid radius of each region is denoted by 'R' and the corresponding area denoted by A. [32]

$$\begin{Bmatrix} r_{eqo} = r_{feo} \\ r_{eqi} = r_{feo} - h_{eq} \end{Bmatrix} \tag{43}$$

Where h_{eq} is the height of iron bridge extending outside the magnet poles. r_{eqo}, r_{eqi} and r_{feo} denotes outer and inner radius of equivalent ring and outer radius of iron core respectively. The centroid radius of the four distinct regions considered is given in equation(44)

$$\begin{Bmatrix} R_1 = \dfrac{2r_{eqo}\sin\dfrac{\beta}{2}}{3\dfrac{\beta}{2}} \\ R_2 = \dfrac{2(r_{eqi} - b_m)\sin\dfrac{\beta}{2}}{3\dfrac{\beta}{2}} \\ R_3 = r_{eqi} - \dfrac{b_m}{2} \\ R_4 = \dfrac{2r_{eqi}\sin\dfrac{\beta}{2}}{3\dfrac{\beta}{2}} \end{Bmatrix} \tag{44}$$

Where R_1, R_2, R_3 and R_4 denotes the centroid radius of four regions in respective order. Equation (45) gives the area of the four regions considered

$$\begin{Bmatrix} A_1 = \dfrac{\beta}{2}{r_{eqo}}^2 \\ A_2 = A_m = \dfrac{\beta}{2}(r_{eqi} - b_m)^2 \\ A_3 = b_m l_m \\ A_4 = \dfrac{\beta}{2}{r_{eqi}}^2 \\ A_{eq} = \dfrac{\beta}{2}(r_{eqo} - r_{eqi})^2 \\ A_{fe} = A_1 - A_2 - A_3 \end{Bmatrix} \tag{45}$$

Where A_1, A_2, A_3, A_4 represents the area of four regions considered in respective order. A_{eq} and A_{fe} denotes the area of equivalent ring and the total area of iron bridge above and on both the sides of the magnet. l_m and b_m represents the length and width of the magnet. Equation (46) calculates the centroid of the iron bridge, magnet and equivalent ring respectively.

$$\begin{Bmatrix} r_{cfe} = \dfrac{R_1A_1 - R_2A_2 - R_3A_3}{A_1 - A_2 - A_3} \\ r_{cm} = R_2 = r_{eqi} - \dfrac{b_m}{2} \\ r_{ceq} = \dfrac{R_1A_1 - R_4A_4}{A_1 - A_4} \end{Bmatrix} \quad (46)$$

Where r_{cfe}, r_{cm} and r_{ceq} denotes centroid radius of iron bridge, magnet and equivalent ring respectively. Finally, equation (47) gives the density of equivalent ring ρ_{eq} and also calculates the tangential stress acting on the equivalent ring σ_{teq}.

$$\begin{Bmatrix} \rho_{eq} = \dfrac{r_{cm}\rho_m A_{m+} r_{cfe}\rho_{fe}A_{fe}}{r_{ceq}} \\ \sigma_{teq} = {r_{ceq}}^2\omega^2\rho_{eq} \end{Bmatrix} \quad (47)$$

3.4 V-shaped Magnet

High torque, power density and wide speed range makes IPM a good choice for motors in electric vehicle. Interior Permanent magnet can be arranged radially, tangentially or at an angle between the poles. In additional, W shaped and U shaped configurations are also possible. The main design challenge in these type of magnets is to optimize the electromagnetic and mechanical performance, which are sometimes conflicting in nature. For example, flux leakage can be reduced thereby improving the electromagnetic performance by reducing the magnet bridge thickness. However, decreasing the bridge thickness negatively affects the mechanical performance. This section studies the theoretical calculations of maximum tangential stress developed in a V-shaped IPM. [33]

As discussed in previous section, equivalent ring calculated based on equivalent mass density is not sufficient to predict the stress for complex structures especially when magnets are arranged at an angle. Centrifugal force is dependent on both mass density as well as radius. Transforming the centrifugal force based on equivalent mass density is not very accurate in V-shaped magnets since the centroid radius is dependent on the angle between the magnet poles. The centroid radius decreases with small angles. Hence, a similar approach to transform centrifugal force based on finding the equivalent radius and equivalent mass density is studied in this section. [33]

In order to calculate the centroid, the magnets are considered as two sections. The iron bridge area is divided into 3 sections based on its geometry as Fe_1, Fe_2 and Fe_3 as shown in Figure 10. [33]

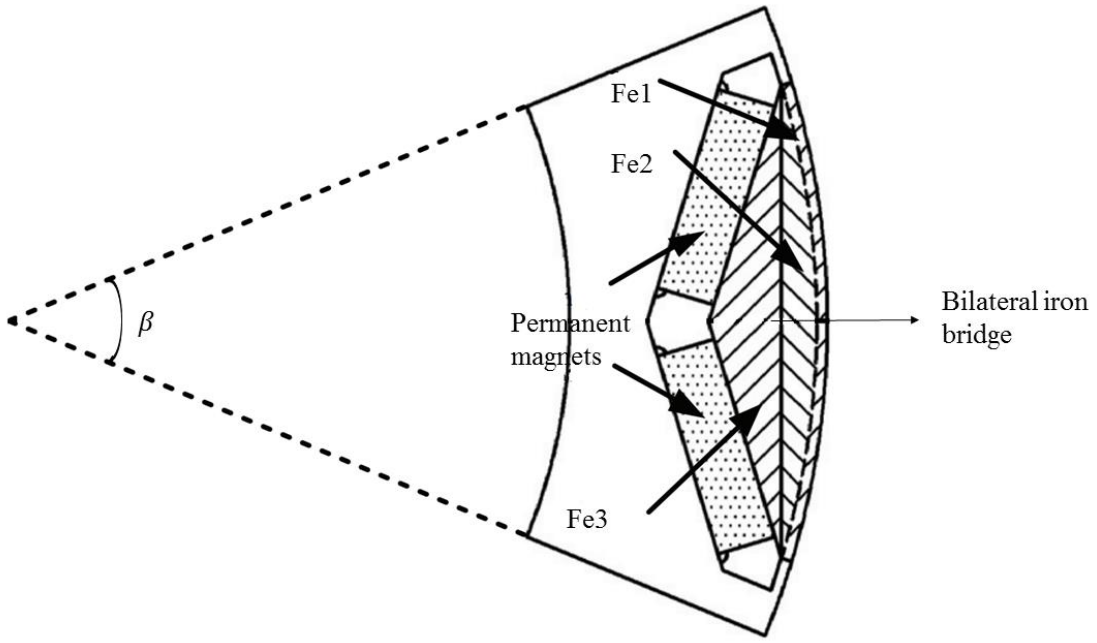

Figure 10. Section view of V-shaped magnet pair [33]

The size of proposed equivalent ring is defined in equation (48)

$$\begin{Bmatrix} r_{eqo} = r_{feo} \\ r_{eqi} = r_{feo} - h_{eq} \end{Bmatrix} \tag{48}$$

Where h_{eq} is the height of iron bridge extending above the magnet poles. r_{eqo}, r_{eqi} and r_{feo} denotes outer and inner radius of equivalent ring and outer radius of iron core respectively. The centroid radius of magnet and iron bridge, R_m and R_{fe}
respectively are given by

$$R_m = r_{eqi}\cos\frac{\beta}{2} - \left\{ r_{eqi}\sin\frac{\beta}{2}\cot\frac{\theta}{2} + \frac{l_m}{2\sin\frac{\alpha}{2}} - \left[\frac{l_m}{2}\cot\frac{\theta}{2} + b_m + \frac{l_m}{2}\right]\cos\frac{\theta}{2} \right\} \tag{49}$$

$$R_{fe} = \frac{\iint_{fe1} x dx + \iint_{fe2} x dx + \iint_{fe3} x dx}{A_{fe1} + A_{fe2} + A_{fe3}} \tag{50}$$

Where, θ is angle between two magnets of a single pole, β is the pole shoe angle, l_m and b_m are the length and breadth of a single magnet. The respective centroid and area of three sections of iron bridge considered given by $\iint_{fe1} x dx$, $\iint_{fe3} x dx$, $\iint_{fe3} x dx$ and A_{fe1}, A_{fe2}, A_{fe3} are defined below.

$$\iint_{fe1} x dx = \frac{2}{3}\left({r_{eqo}}^3 - {r_{eqi}}^3\right)\sin\beta \tag{51}$$

$$\iint_{fe2} x dx = \frac{2}{3} r_{eqi}\left[\sin\frac{\beta}{2} - \cos^3\frac{\beta}{2}\tan\frac{\beta}{2}\right] \tag{52}$$

$$\iint_{fe3} x dx = {r_{eqi}}^3\left[\sin^2\frac{\beta}{2}\cos\frac{\beta}{2}\cot\frac{\theta}{2}\right] \tag{53}$$

$$A_{fe1} = \beta\left({r_{eqo}}^2 - {r_{eqi}}^2\right) \tag{54}$$

$$A_{fe2} = \frac{1}{2}{r_{eqi}}^2[\beta - \sin\beta] \tag{55}$$

$$A_{fe3} = {r_{eqi}}^2\sin^2\frac{\beta}{2}\cot\frac{\theta}{2} \tag{56}$$

Where r_{eqi} and r_{eqo} represents the inner and outer radius of the proposed equivalent ring. Equivalent mass density ρ_{eq} is given by

$$\rho_{eq} = \frac{\left(R_m\rho_m A_m + R_{fe}\rho_{fe}A_{fe}\right)\frac{1-\cos\theta}{2}}{R_o A_{eq}} \tag{57}$$

Where ρ_{fe} and ρ_m correspond to the respictive densities of iron bridge and magnet. A_m is the total area of two magnets and A_{fe} is the total area of iron bridge.

$$A_m = 2l_m b_m \tag{58}$$

$$A_{fe} = A_{fe1} + A_{fe2} + A_{fe3} \tag{59}$$

Area of the equivalent ring A_{eq} is given by

$$A_{eq} = A_{fe1} \tag{60}$$

The centroid radius of equivalent ring R_{eq} is given by

$$R_{eq} = \frac{r_{eqo} + r_{eqi}}{2} \tag{61}$$

Circumferential or tangential stress is given by

$$\sigma_t = {R_{eq}}^2 \omega^2 \rho_{eq} \tag{62}$$

Maximum tangential stress is given by

$$\sigma_{tmax} = SF\sigma_t \tag{63}$$

Where SF is the stress concentration factor which can be deduced from Finite element analysis test cases.

4 GEOMETRY, THERMAL AND SPEED TEST OF PERMANENT MAGNET ROTORS

A systematic approach is followed in this study to analytically calculate the mechanical stress in high speed permanent magnet rotors and to further verify the results using a tool based on finite element method. The simplest and ideal structure consisting of a continuous cylindrical permanent magnet is studied first followed in order by more complex magnet shapes like SPM, IPM and V-shaped magnets. The mathematical formulas are coded in Matlab 2017 and the results are verified in Ansys 18. In the first two methods, radial, tangential and Von Mises stress are plotted along the radial length of the rotor assembly, whereas only the maximum tangential stress is calculated for the last two methods.

The accuracy of the obtained result is found by an error analysis of the Matlab result by comparing the same with corresponding Ansys results. Multiple experiments are conducted for the same model to ensure reliability of obtained results. Geometry test, thermal test and speed tests are performed for the first model. However, only geometry and speed test are performed on the results of the remaining three models. Reliability is ensured by continuing the experiments until consistent error percentage is attained under different test data. Saturation of test results is also taken care in this study by converging the finite element results with multiple test runs. In each test, different type and density of mesh is used till the results converge to a fine point.

The geometry, materials and test conditions used for the four different methods corresponding to four types of permanent magnets studied are discussed here followed by their corresponding test results. In case of CPM and IPM tests, Matlab results are reported first as stress plots, followed by Ansys results. It is succeeded by a comparison study which expounds the accuracy of the Matlab code by determining the error percentage in the code as compared against the Ansys results. Matlab plots are absent in the test results of IPM and VPM study since the code for these two methods calculates only the maximum tangential stress. In the IPM and VPM test results, Ansys results are reported first followed by an error analysis which tabulates Matlab results, Ansys results and their corresponding error percentage.

4.1 Geometry test on cylindrical permanent magnet

Matlab code for analytical stress calculation of CPM structure is developed based on the theory of rotating cylinders given by Hearn in the book “Mechanics of materials 2” [24]. The stress analysis includes two loading conditions, one due to rotational speed and other one due to shrink fit between rotor core and magnet as well as that between magnet and the enclosure. The code calculates stress variation along a radial line ranging from center of rotor core to the outer diameter of the enclosure. Due to the symmetry of the cylindrical structure, it is assumed that the stress variation along the radial line does not vary across the circumference. Moreover, shear stress is assumed to be zero due to geometric symmetry.

The reliability of code developed to calculate the radial, tangential and von Mises stress in CPM structure is tested by studying three different geometric variations of the rotor assembly. The rotor assembly consist of a steel core, cylindrical permanent magnet and an enclosure. The shaft as well as lamination is considered as a single entity in this study. Geometry is varied by incrementing the diameter of all the components uniformly by 10 mm in each test. The material data used for the geometry test is given in Table 1

Table 1. Material data for geometry test of CPM

Material Property	Core (Stainless Steel)	PM (NdFeB)	Enclosure (Carbon Fiber)
Density (Kg/m^3)	7850	7400	1800
Elastic Modulus (GPa)	210	160	228
Poissons Ratio	0.3	0.24	0.32
CTE ($*10^{-6}$) (/°C)	12	8	13
Yield Strength (MPa)	335	120	NA
Ultimate strength (MPa)	NA	NA	600

Stainless steel is the material selected for the rotor core including shaft and lamination. The permanent magnet is made of neodymium iron boron (NdFeB) and the enclosure is made of carbon fiber. It is to be noted that, carbon fiber is an orthotropic material whose material property varies in different directions. But, the orthotropic nature of carbon fiber material is

not taken into account in this study. Instead, a constant value is assigned for all the properties in the Matlab code as well as in the Ansys material definition table. CTE in the table refers to the material property coefficient of thermal expansion.

The continuous cylindrical structure makes it possible to shrink fit the magnet to the core as a means of mechanical fastening. Shrink fit is also provided between the magnet and the enclosure to resist the high centrifugal forces. General parameters like the rotational speed, interference, thermal gradient between rotor and the ambient temperature and the number of simulation steps used in Matlab code to divide the radial length equally are listed in Table 2.

Table 2. General parameters for geometry test of CPM

Rotational velocity (rpm)	15000
Interference fit (μm)	100
Thermal gradient (℃)	0
Matlab simulation steps	300

Three consecutive tests are done for three different geometries namely geometry test 1, geometry test 2 and geometry test 3. The diameter of each component is incremented by 10 mm in each consecutive test case. Table 3 lists the dimensions of rotor core, magnets and the enclosure for geometry test 1

Table 3. Dimensions of components for geometry test 1 of CPM

Geometry	Core (Stainless Steel)	PM (NdFeB)	Enclosure (Carbon Fiber)
Inner Radius (mm)	0	35.5	40.5
Outer Radius (mm)	35.5	40.5	42.5

The Matlab plots for radial, tangential and von Mises stress for the first geometry is shown in Figure 11 .

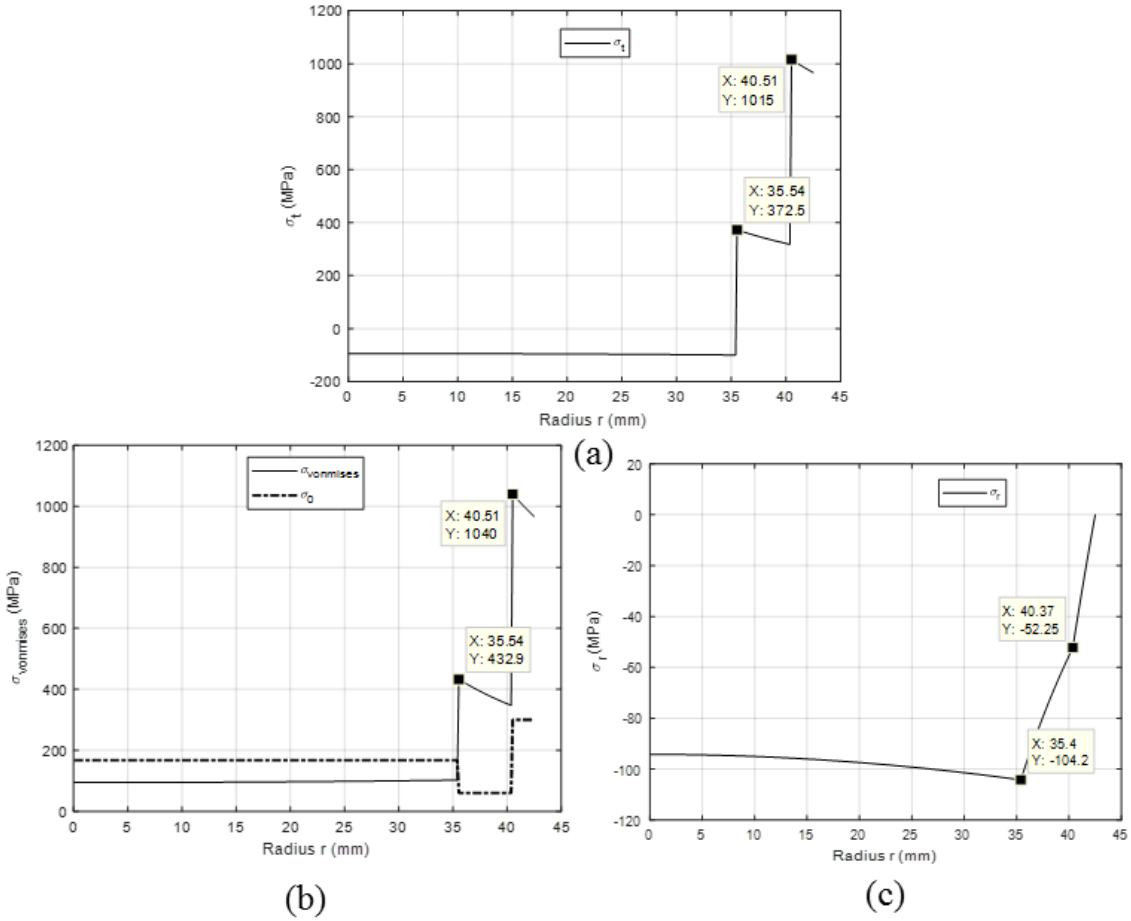

Figure 11. Matlab stress plots for CPM geometry test 1. (a)Tangential stress plot, (b) radial stress plot, (c) von Mises stress plot

As seen from Figure 11, radial stress is in the shrink fit assembly is mostly compressive in nature, while tangential stress is tensile. The contact between shaft and magnet has to be intact in order to transfer the torque to the shaft adequately. The shrink fit provides a negative compressive stress in the contact region which mainly accounts for radial stress to be in negative region. But the stress induced in the rotating components due to centrifugal action is tensile. Moreover, the centrifugal stress is directly proportional to the square of radius. Hence, the centrifugal stress reduces the compressive stress by adding up tensile stress component. This explains increase in radial stress with the increase in radius. In the outermost radius which corresponds to the external diameter of enclosure, radial stress is zero due to the absence of physical constrains which prevent free expansion or contraction of material.

In case of a shrink fitted assembly, the tangential stress induced is compressive for inner component while it is tensile for the outer component. Meanwhile, the tangential stress induced due to centrifugal forces are always positive. While considering the first contact region between the rotor core and the magnet, tangential stress due to shrink fit is positive while that due to centrifugal force is negative. These two components cancel out partially in case of the inner component which is the rotor core. However, tangential stress due to interference as well as due to centrifugal force is positive for the outer component which is the magnet. Hence, these two components add up which leads to the tangential stress peak in the first contact region between rotor core and magnet. The tangential stress peak in the second contact region between magnet and enclosure can also be explained by the same reason.

The Matlab results are verified using finite element analysis done in Ansys. Ansys model is created with similar geometry and material properties as defined in the code for Matlab. The contact between the different components are selected appropriately and the mesh type and mesh density is finalized after repeated test runs. The input data used for finite element analysis (FEA) is listed in Table 4. The contact type between the contact surface is chosen as frictional which better defines the scenario studied here. Frictional surface prevents relative sliding between components and develop shear forces between interacting surfaces. As already mentioned in the assumptions, the shear force is neglected due to the symmetry of the structure which cancel outs the developed shear forces and hence is no accounted in analytical calculation. Different coefficient of friction between 0.1 and 0.2 were experimented without significant deviation in results and finally friction coefficient of 0.2 is chosen and used across all the models studied in this thesis. The geometry and mesh type used for the model is clarified in Figure 12, Figure 13 and Figure 14.

Table 4. FEA model details for geometry test of CPM

Magnet Configuration	Continuous cylindrical
Mesh Type	Proximity
Mesh size	Medium
Core-Magnet contact type	Frictional (0.2)
Enclosure-Magnet contact type	Frictional (0.2)

Figure 12 shows the radial stress plot in Ansys for the first geometry test. The left side of figure illustrates the mesh quality and the stress distribution of the enclosure and magnet at top and bottom respectively. The right side of the figure displays an exploded view of entire assembly illustrating the mesh size and stress distribution. Stress from the midpoint of both the contact regions are taken for comparison with the Matlab results.

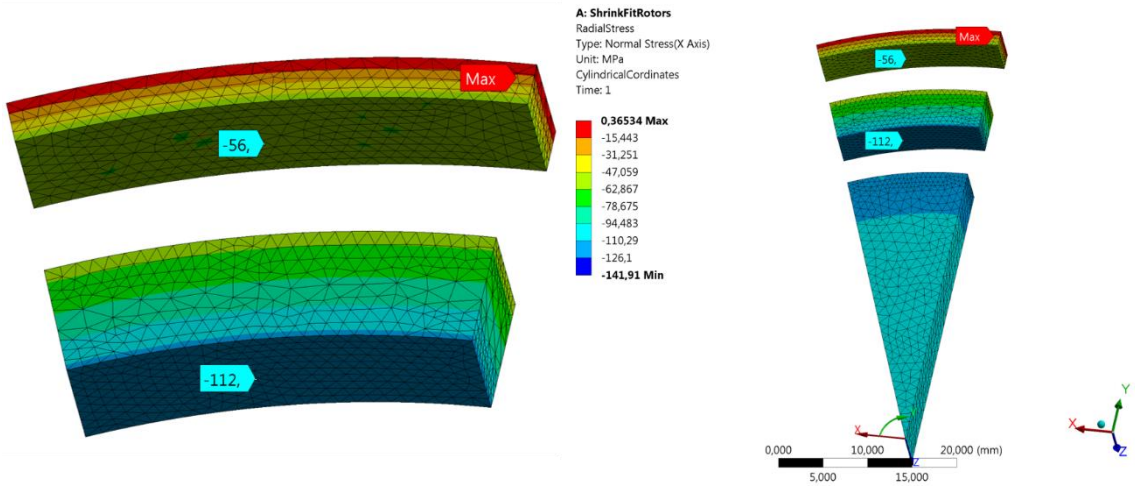

Figure 12. Radial stress plot in Ansys for CPM geometry test 1

As seen from Figure 12, FEA result agrees with the Matlab result for stress variation along the radius. The exact values of stress have some error percentage in comparison with FEA, which is detailed in Table 5. The tangential stress distribution for the Ansys model is shown in Figure 13. As in the previous case, the left side of figure illustrates the mesh and stress distribution of enclosure and magnet respectively at top and bottom, while the right hand side shows an exploded view of the entire assembly.

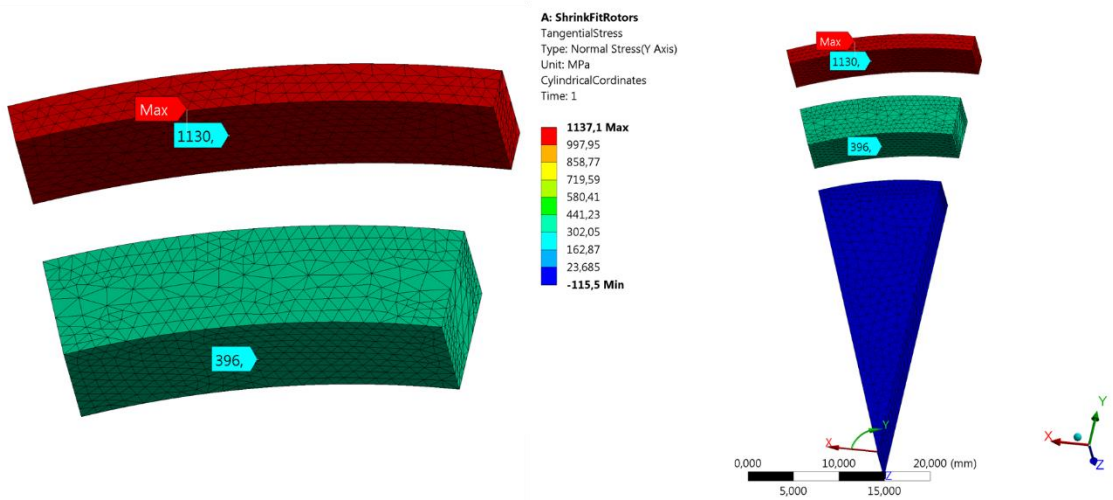

Figure 13. Tangential stress plot in Ansys for CPM geometry test 1

The von Mises stress distribution for the Ansys model is shown in Figure 14. It is obvious from Figure 13 and Figure 14 that tangential stress is the most prominent stress in the model. The maximum von Mises stress is lower than the maximum tangential stress.

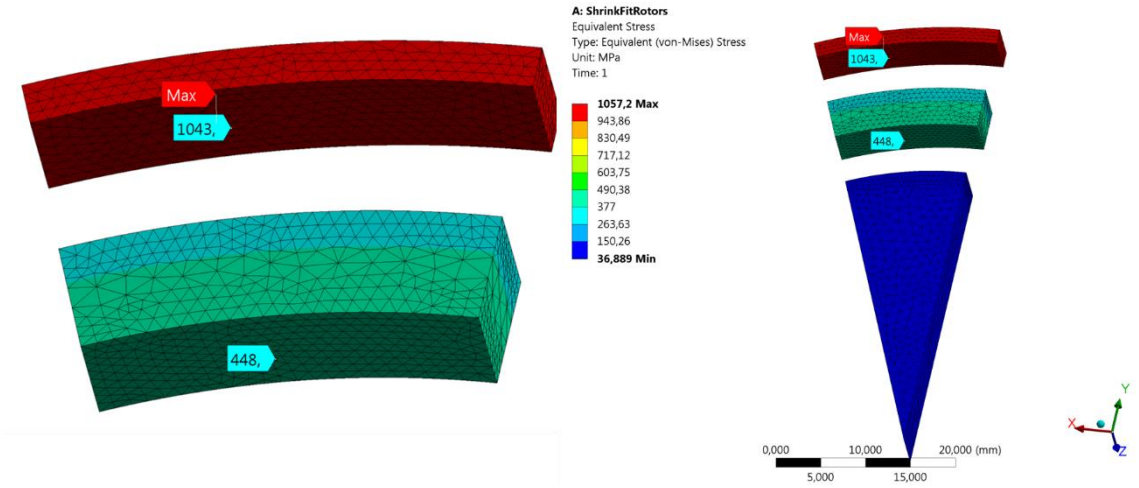

Figure 14. Von Mises stress plot in Ansys for CPM geometry test 1

Table 5 compares the Matlab and FEA results at three points, the contact between rotor core and magnet, contact between magnet and enclosure and finally the maximum stress. The percentage of error in Matlab result as compared against FEA result is also tabulated.

Table 5. Error analysis of CPM geometry test 1

Rotor-Magnet contact		Fe stress (MPa)	Matlab stress (MPa)	Error (%)
	Radial stress	112	104	7.14
	Tangential stress	396	373	5.81
	Von Mises stress	448	433	3.35
Magnet-Enclosure contact	Radial stress	56	52	7.14
	Tangential stress	1130	1015	10.18
	Von Mises stress	1043	1040	0.29
Maximum Stress	Radial stress	112	104	7.14
	Tangential stress	1130	1015	10.18
	Von Mises stress	1043	1040	0.29

It is observed from Table 5 that while the error in radial stress maintains a constant pattern, the tangential and von Mises stress looks slightly inconsistent in their variation at different points. A better analysis is possible only by doing more test cases.

The second geometry test is done by incrementing 10 mm to the dimensions of all components from geometry test 1. Table 6 lists the dimensions of the geometry used in Matlab code as well as for the Ansys model.

Table 6. Dimensions of components for geometry test 2 of CPM

Geometry	Core (Stainless Steel)	PM (NdFeB)	Enclosure (Carbon Fiber)
Inner Radius (mm)	0	40.5	45.5
Outer Radius (mm)	40.5	45.5	47.5

All other parameters except the geometry remains unchanged from geometry test 1. Hence, the material data and model details from Table 1and Table 2 are used in this experiment as well. Moreover, the mesh used for this experiment is similar to that illustrated in Figure 12, Figure 13 and Figure 14. The test results for geometry test 2 is presented in Table 7.

Table 7. Error analysis of CPM geometry test 2

Rotor-Magnet contact		Fe stress (MPa)	Matlab stress (MPa)	Error (%)
	Radial stress	88	81	7.95
	Tangential stress	356	336	5.62
	von Mises stress	391	383	2.05
Magnet-Enclosure contact	Radial stress	45	41	8.89
	Tangential stress	1020	916	10.20
	von Mises stress	939	935	0.43
Maximum Stress	Radial stress	88	81	7.95
	Tangential stress	1020	916	10.20
	von Mises stress	939	935	0.43

A comparison between Table 5 and Table 7 reveals that the error percentage at different locations follows a close pattern between different geometries. The radial error percentage lies around 7% and 8% percentage, the tangential stress error percentage for the first contact region is around 5% while it is around 10% for the second contact region for both the geometries. The error percentage for von Mises stress at the contact between rotor core and magnet are around 2% and 3% in both the tests, while the maximum von Mises stress which occurs at the magnet enclosure contact is less than 1% in both the cases.

The error pattern is finalized by doing one more test in which all the parameters are kept same as in the first two test cases except the geometry. The data regarding geometry of the different components are listed in Table 8. Material data and model details can be referred from Table 1and Table 2 respectively.

Table 8. Dimensions of components for geometry test 3 of CPM

Geometry	Core (Stainless Steel)	PM (NdFeB)	Enclosure (Carbon Fiber)
Inner Radius (mm)	0	45.5	50.5
Outer Radius (mm)	45.5	50.5	52.5

The test results for geometry test 3 is given in Table 9. Matlab results and FEA results are successively followed by an error analysis in the table.

Table 9. Error analysis of CPM geometry test 3

Rotor-Magnet contact		Fe stress (MPa)	Matlab stress (MPa)	Error (%)
	Radial stress	70	65	7.14
	Tangential stress	324	305	5.86
	von Mises stress	348	337	3.16
Magnet-Enclosure contact	Radial stress	37	34	8.11
	Tangential stress	929	836	10.01
	von Mises stress	852	852	0.00
Maximum Stress	Radial stress	70	65	7.14
	Tangential stress	929	836	10.01
	von Mises stress	852	852	0.00

The error percentage shows a consistent pattern while comparing the corresponding error data for three geometry tests as is seen from Table 5, Table 7 and Table 9.

4.2 Thermal test on cylindrical permanent magnet

Thermal test is done to verify whether the developed Matlab code provides reliable results under a thermal gradient between the rotating components and ambient temperature. In practical scenario, thermal behavior of materials is nonlinear in nature. But, a constant thermal gradient between the entire rotor assembly and ambient temperature is considered in this study. Moreover, the CTE is assumed as a constant for all materials and do not vary based on temperature. It is to be noted that the basic equation of thermal strain which is the product of CTE and thermal gradient is used in this study. The change in diameter due to thermal strain is added in the respective diameters while defining the geometry of each component in the Matlab code. Apart from this, thermal stress is not considered separately in any of the analytical calculations.

Two tests are done in this section, one with zero thermal gradient and the other one with 100 degree Celsius as the thermal gradient. The dimensions of components used for the thermal test is selected based on the geometry test 2 and the corresponding data is listed in Table 6. The material data used for the thermal test is same as that listed in Table 1 for both the tests.

The general parameters used for thermal test 1 is same as that provided in Table 2. Thermal test 2 also uses the same parameters listed in Table 2 except for a change in thermal gradient which is 100 degree Celsius. The FEA data used in both the thermal tests are same as listed in Table 4.

Since the thermal test 1 performed at zero thermal gradient produces the same result as that of geometry test 2, the results are not repeated here again. Thermal test 2 is a repetition of thermal test 1 with 100 degree Celsius as thermal gradient. The radial, tangential and von Mises stress plots in Ansys for thermal test 2 is given in Figure 15, Figure 16 and Figure 17 respectively.

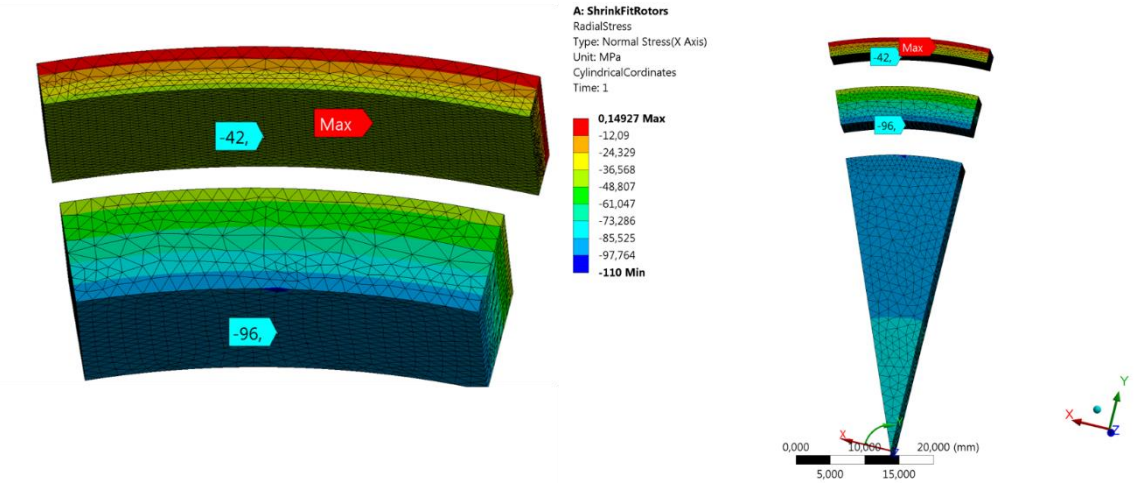

Figure 15. Radial stress plots for thermal test 2 at a thermal gradient of 100 degree Celsius

The stress values from the mid point of contact surface is chosen for comparison instead of the local maximum. A comparison of data from Figure 15 to the corresponding FEA data in Table 7 gives the change in stress distribution in CPM assembly when the temperature in the rotor rises to 100 degree Celsius above the ambient temperature. The FEA trend shows that, while the compressive stress between the magnet and rotor core increases with temperature rise, the compressive stress between magnet and enclosure almost remains same and drops only by 3 MPa.

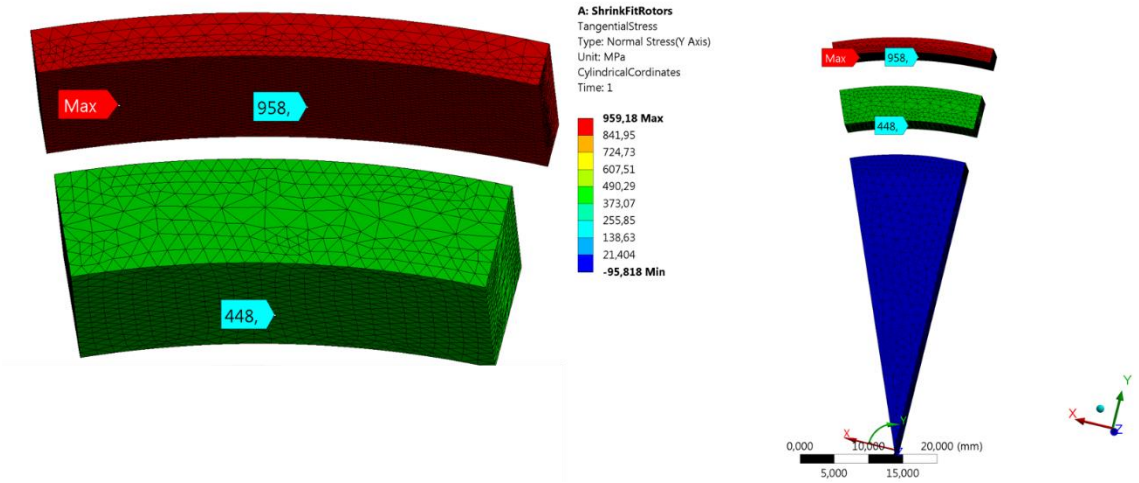

Figure 16. Tangential stress plots for thermal test 2 at a thermal gradient of 100 degree Celsius

Figure 16 is compared with Table 7 for their corresponding FEA stress values at different locations. The same trend in radial stress comparison is repeated here as well. The tangential stress between rotor magnet contact increases while that between magnet enclosure contact increases.

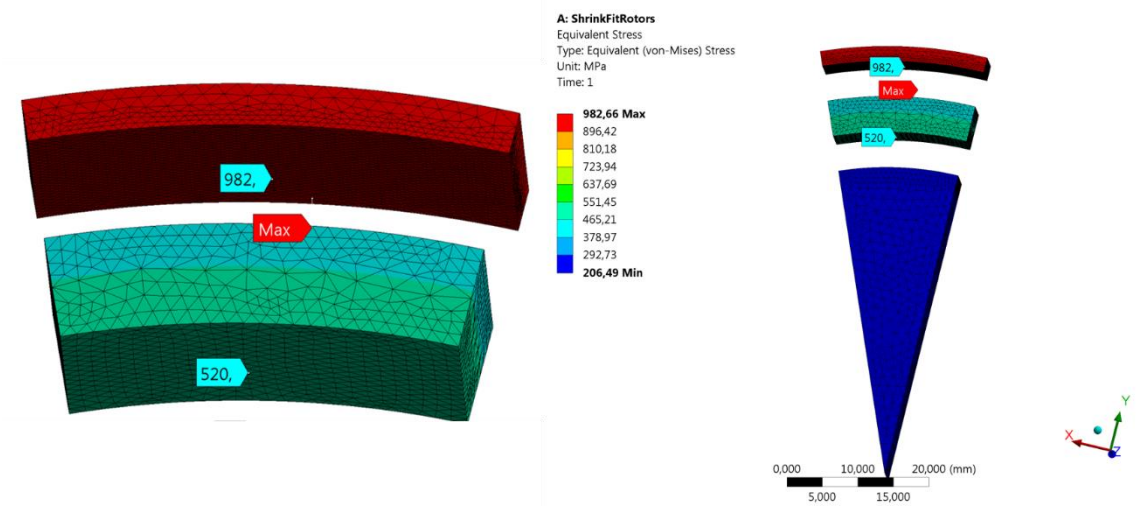

Figure 17. von Mises stress plots for thermal test 2 at a thermal gradient of 100 degree Celsius

von Mises stress values at both contact region seems to increase when stress points from Figure 17 is compared against corresponding FEA data listed in Table 7. A detailed comparison is provided in Table 10 which compares the FEA stress data from the above Ansys plots with the corresponding values obtained from the Matlab test.

Table 10. Error analysis of thermal test 2 at a thermal gradient of 100 degree Celsius

Rotor-Magnet contact		Fe stress (MPa)	Matlab stress (MPa)	Error (%)
	Radial stress	96	88	8.33
	Tangential stress	448	404	9.82
	von Mises stress	520	453	12.88
Magnet-Enclosure contact	Radial stress	42	40	4.76
	Tangential stress	958	887	7.41
	von Mises stress	982	905	7.84
Maximum Stress	Radial stress	96	88	8.33
	Tangential stress	958	887	7.41
	von Mises stress	982	905	7.84

Table 7 and Table 10 are compared to study the trend followed by Matlab and FEA results when a thermal gradient is introduced to the model. It is inferred from the comparison that Matlab results follows the same trend of FEA results for radial and tangential stress, even though the exact stress values and hence the error percentage varies slightly. But, in the case of von Mises stress, the trend in Matlab results contradicts with the corresponding trend in FEA results. Despite the fact that all the stress values in FEA results increases with introduction of thermal gradient, an increase in the von Mises stress in Matlab results is observed only at rotor magnet contact while that at magnet enclosure contact decreases.

4.3 Speed test on cylindrical permanent magnet

In speed test, one Ansys model is tested under 5 varying rotational speeds from 10000 to 30000 rpm with an increment of 5000 rpm between each consecutive test. All other parameters except the speed are kept constant both in FEA as well as in the Matlab code input data. The error percentage is calculated based on the variation with the FEA results which is then tabulated to find the mean error percentage. The closeness of error value of each test to the mean error determines the reliability of the studied method. Moreover, the mean error can be utilized to find a correction factor that can be applied to the Matlab code

The material data used in the speed test is same as that listed in Table 1. The general parameters used in the geometry test except for the rpm are also used in speed test which is referred in Table 2. In addition, the FEA also uses the same data as referred in Table 4. The geometry selected for the speed test corresponds to that of second geometry test and the dimensions of components are already listed in Table 6. The tangential stress is plotted for different speeds in Matlab and is presented in Figure 18.

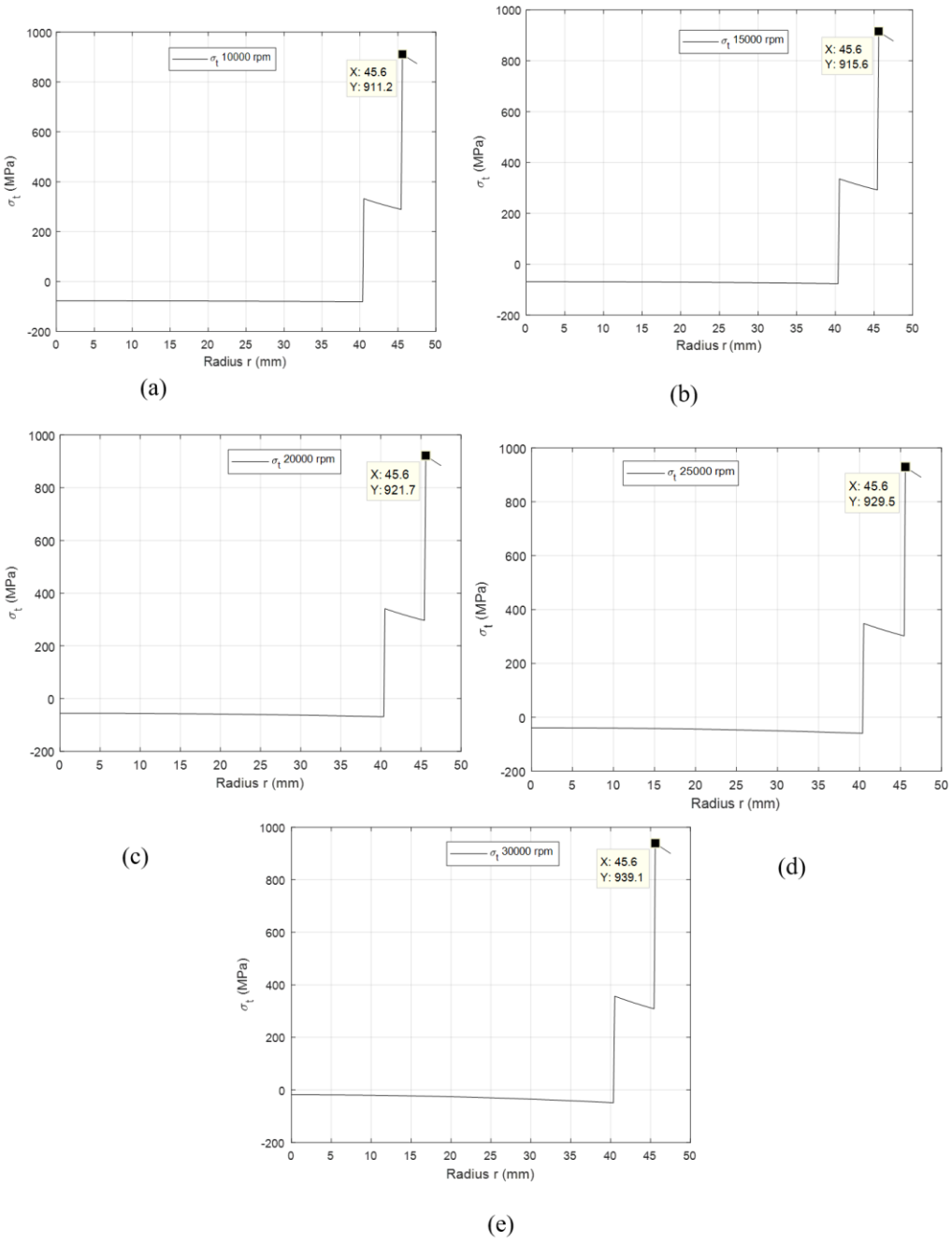

Figure 18. Tangential stress plotted in Matlab for speed test on CPM. (a) 10000 rpm, (b) 15000 rpm, (c) 20000 rpm, (d) 25000 rpm, (e) 30000 rpm

It is evident from Figure 18 that the stress peak occurs in the magnet enclosure contact region. Moreover, the peak stress increases with an increase in speed as is expected. This stress peak for each test is compared with stress values taken from similar location in a FEA model as shown in Figure 19

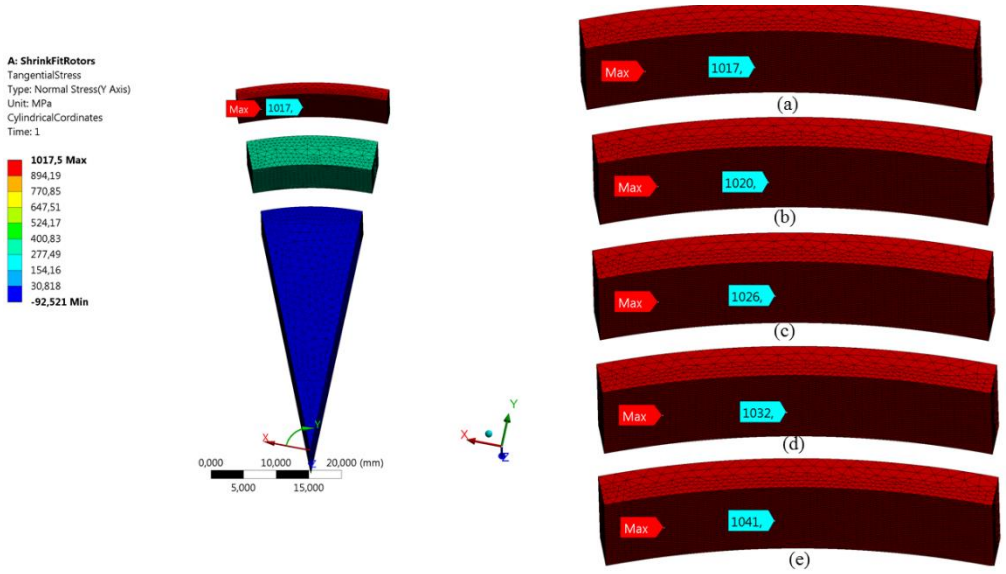

Figure 19. Tangential stress plots in Ansys for CPM speed test. (a) 10000 rpm, (b) 15000 rpm, (c) 20000 rpm, (d) 25000 rpm, (e) 30000 rpm

The stress peaks are taken from the center of the contact region instead of the local stress peak for comparison. Moreover, the values obtained are round off to zero decimal places in case of both the results. Table 11 compares the Matlab and FEA results for maximum tangential stress taken form the contact region between magnet and enclosure.

Table 11. Error analysis of CPM speed test

RPM	Fe Stress (MPa)	Matlab Stress (MPa)	Error (%)
10000	1017	911	10.42
15000	1020	916	10.20
20000	1026	922	10.14
25000	1032	930	9.88
30000	1041	939	9.80
Mean error			10.09

It is apparent from Table 11 that the error percentage shows minimum deviation over the range of experiments with a maximum variation of 0.33% from the mean value which occurs in the case of minimum speed of 10000 rpm.

4.4 Geometry test on surface permanent magnet

SPM structure consist of permanent magnets arranged along the surface of the rotor core. Laminations are not considered separately in this study. Instead, the lamination is integrated with the shaft to form a single entity. Even though, the surface magnets can be arranged in two different forms, one being segmented magnets and other being separated by a filler material, only one approach is followed in this study. The magnets in the tested Ansys model is separated by a filler material made of aluminum alloy. A bandage or enclosure made of titanium alloy encloses the surface magnets and prevent them from flying off under high surface velocities.

FEA of the model with varying geometry and speeds converged to the conclusion that the tangential stress is the most prominent among radial, tangential and von Mises stress in SPM structure. Moreover, the maximum tangential stress occurs in the enclosure above the separation material, in the space between adjacent magnets. The Matlab code developed for this study is an extension of the first method used for cylindrical permanent magnet. Tangential stress is plotted along the radius of the rotor assembly at a radial line including the rotor core, PM and enclosure. The two loading conditions are rotational speed and interference fit between PM and enclosure. The analytical model for the contact surface between the magnet and the separation material is not studied here. This limiting factor affects the maximum stress above the magnet. In addition, the peak stress above the magnet rig cannot be predicted by this approach. Therefore, a correction factor (CF) is included in the Matlab code to predict the maximum stress which will subjugate the above mentioned limiting factor. Furthermore, a stress concentration factor (SCF) is employed in the Matlab code to predict the peak stress above the separation rig. The CF and SCF are determined based on the error analysis on comparison with FEA study. The mean error from different tests helps to calculate both the factors.

Three different geometries of SPM are studied in this section for analyzing the stress variation. The diameter of rotor core is increased by 10 mm in each case which consequently

varies the diameter of magnet and enclosure. The thickness of the enclosure and magnets are not changed. Magnet thickness is maintained at 5 mm and enclosure thickness is maintained at 2 mm for all the three cases. The material data used in the Matlab code and Ansys model is listed in Table 12.

Table 12. Material data for geometry test of SPM

Material Property	Core(S350)	PM (NdFeB)	Enclosure (Ti-6Al-4V)	Magnet rig (7075-T6)
Density (kg/m^3)	7850	7400	4471	2810
Elastic Modulus (GPa)	210	160	115	210
Poissons Ratio	0.3	0.24	0.342	0.3
CTE ($*10^{-6}$) (/°C)	12	8	9.5	25.5
Yield Strength (MPa)	350	120	250	350
Ultimate strength (MPa)	NA	NA	NA	700

Thermal gradient is ignored in this test. The general parameters for geometry test of SPM is given in Table 13.

Table 13. General parameters for geometry test of SPM

Rotational velocity (rpm)	15000
Interference fit(μm)	100
Thermal gradient(°C)	0
Matlab simulation steps	300

A section of SPM structure is modelled in Ansys such that it includes half of two adjacent magnets on both the sides of the aluminum test rig used as filler material in this study. While the enclosure magnet contact is modelled as frictionless in the Ansys model, the contacts between magnet and rotor core and the one between magnet and rig material is modelled as frictional with a friction coefficient of 0.2. The FEA parameters are listed in Table 14.

Table 14. FEA model details for speed test of SPM

Magnet Configuration	4 pole Surface permanent magnet
Mesh Type	Curvature
Mesh size	Medium
Core-Magnet contact type	Frictional (0.2)
Enclosure-Magnet contact type	Frictionless
Magnet Rig-Magnet contact	Frictional(0.2)

The mesh density and final stress distribution in Ansys model can be observed from Figure 20. The left side of figure gives the exploded view of rotor assembly in Ansys for the first geometry studied here. The lower portion of exploded assembly included the core, magnets and filler mterial which is hard to distinguish due to similar color blue for all the regions. This is because the stress in enclosure is very high compared to all other regions and hence minor stress variations in other regions are coded in same color in Ansys. The right side of figure shows the stress distribution in enclosure for the three geometries arranged in ascending order of diameters. The stress point at the middle denotes the stress above filler material and on the two sides represents the stress above two adjacent magnets taken from their middle region.

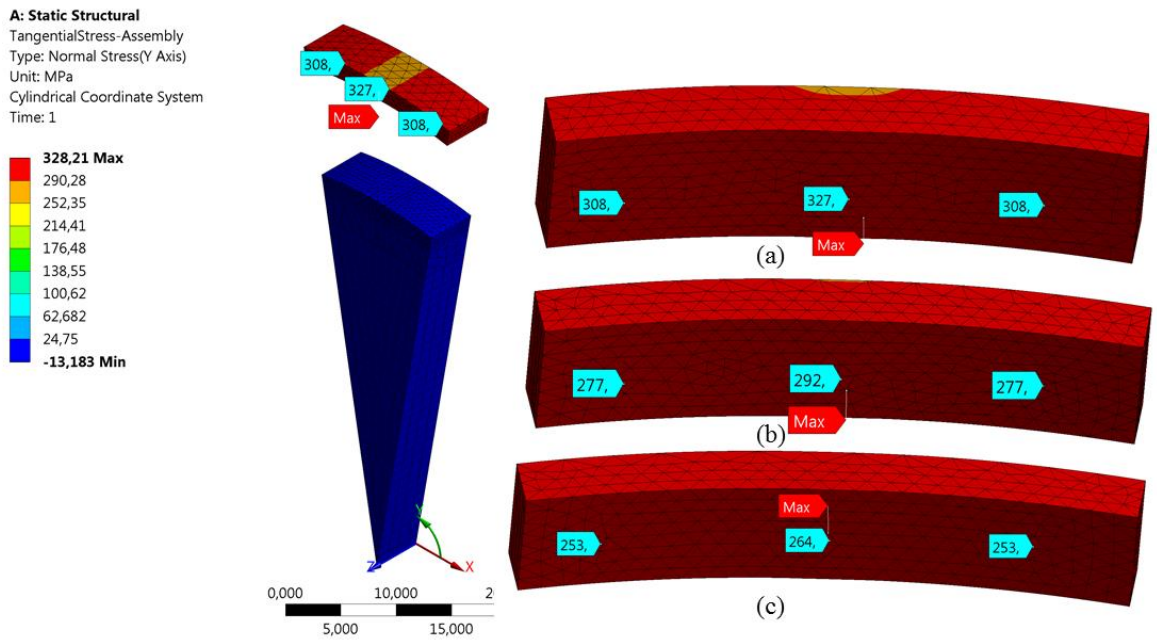

Figure 20. Tangential stress plots in Ansys for SPM geometry test. a) Rotor core diameter of 71 mm, b) Rotor core diameter of 81 mm, c) Rotor core diameter of 91 mm

The results from Matlab code is listed in Table 15 along with a comparison with the FEA results in Ansys. An error percentage is calculated in the last column of the table which indicates the deviation of Matlab results from the FEA results which is used as the reference here.

Table 15. Error analysis of SPM geometry test

Rotor core diameter (mm)	Fe Stress (MPa)		Matlab Stress (MPa)		Error %	
	Stress above magnet	Peak stress	Stress above magnet	Peak stress	Stress above magnet	Peak stress
71	308	327	277	277	10.06	15.29
81	278	293	248	248	10.79	15.36
91	253	264	226	226	10.67	14.39
Mean error percentage					10.51	15.01

Peak stress in Table 15 refers to the stress above the filler material where the maximum stress occurs. It is observed that the stress above magnet shows a consistent error percentage across the different test cases. The error deviation between the maximum and minimum error percentage is 0.73 % with a mean error of 10.51 %. The peak stress also looks reliable with not much deviation between the error percentages between different test cases.

4.5 Speed test on surface permanent magnet

The first geometry in the SPM geometry test is selected to do a speed test where the geometry and all other parameters in Matlab code and Ansys model are kept constant by varying the rotational velocity from 10000 to 30000 rpm. The material data for speed test of SPM is given in Table 12. Table 16 lists the dimensions of the constituting components of SPM structure. The axial length is assumed to be unity. The separation material named as magnet rig or filler material is a 2mm wide section cut from a disc whose inner and outer diameters are same as that of the magnet. Tangential stress variation along the inner radius of rotor core to outer radius of enclosure along the region of magnet is considered for the stress calculation. As stated previously, the region comprising of magnet rig which separates adjacent magnet has different material properties which are not accounted in this experiment. The properties of contact region between magnet and rig is also ignored.

Table 16. Dimensions of components for speed test of SPM

Geometry	Core(S350)	PM (NdFeB)	Enclosure (Ti-Alloy)	Magnet rig (7075-T6)
Inner Radius (mm)	0	35.5	40.5	35.5
Outer Radius (mm)	35.5	40.5	42.5	40.5
Width (mm)	NA	NA	NA	2

The Matlab test results are presented in Figure 21.

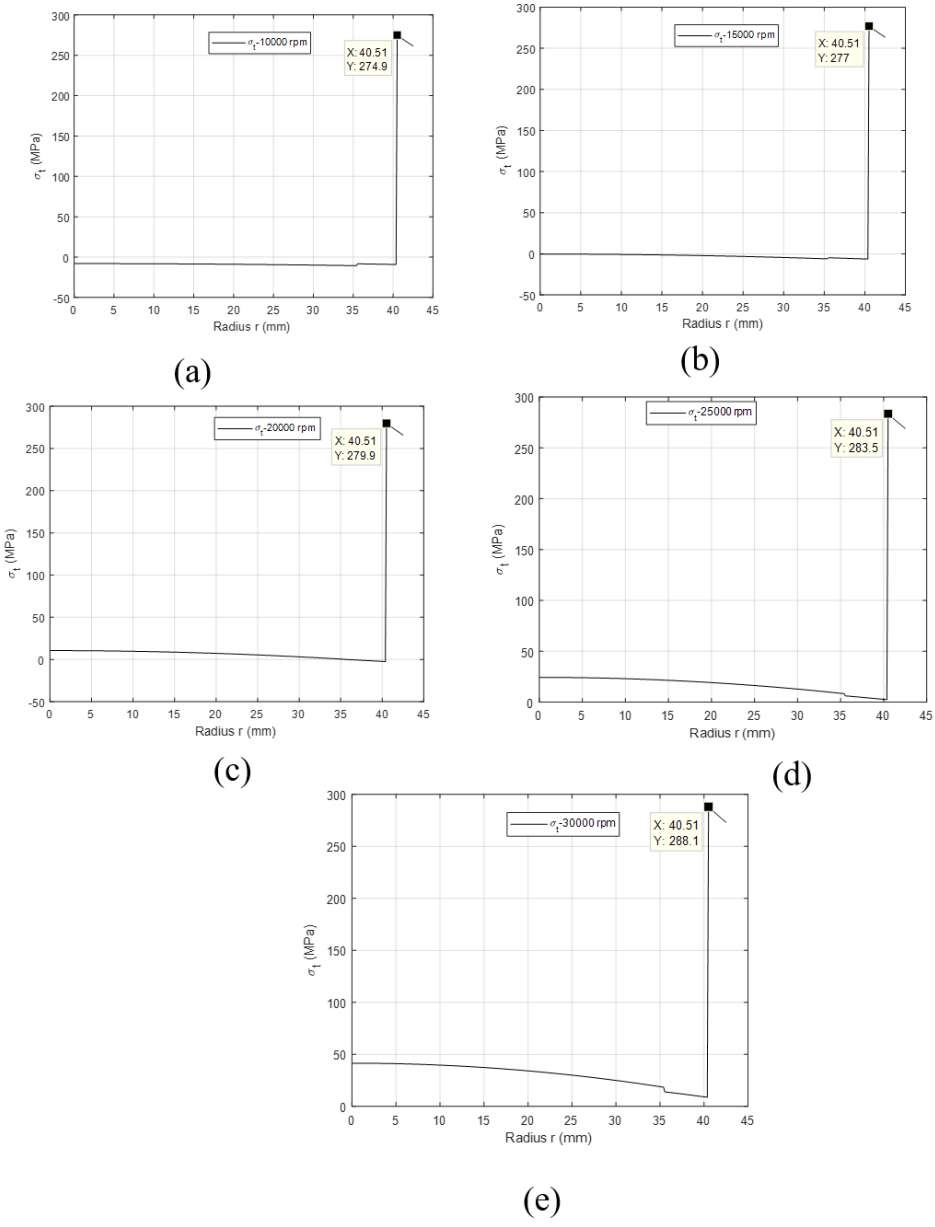

Figure 21. Tangential stress plots in Matlab for SPM speed test. (a) 10000 rpm, (b) 15000 rpm, (c) 20000 rpm, (d) 25000 rpm, (e) 30000 rpm

The stress plots in Ansys is demonstrated in Figure 22. A 20 degree angular section is studied here which comprises of two magnet sections and a magnet rig or filler material separating them. Stress values at the inner side of enclosure are taken from three points, mid point of two magnets and mid point of the magnet rig.

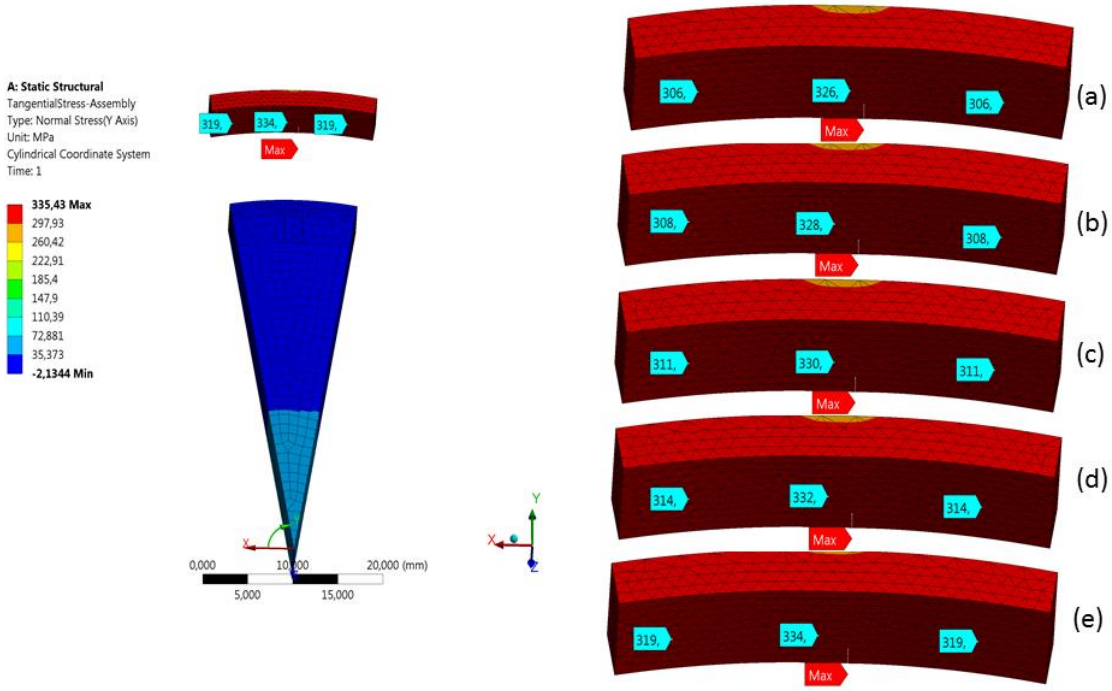

Figure 22. Tangential stress plots in Ansys for SPM speed test. (a) 10000 rpm, (b) 15000 rpm, (c) 20000 rpm, (d) 25000 rpm, (e) 30000 rpm

It is obvious from Figure 22 that the stress peak occurs above the magnet rig whose value is greater than that above magnets. The stress above magnets taken from the midpoint of both sides coincides which implies that the stress results chosen are reliable enough. Table 17 makes a comparison between Matlab and Ansys results for tangential stress in the enclosure above magnet and also takes into account the peak stress.

Table 17. Error analysis of SPM speed test

RPM	Fe Stress (MPa)		Matlab Stress (MPa)		Error %	
	Stress above magnet	Peak stress	Stress above magnet	Peak stress	Stress above magnet	Peak stress
10000	306	326	275	275	10.13	15.64
15000	308	325	277	277	10.06	14.77
20000	311	330	280	280	9.97	15.15
25000	314	332	284	284	9.55	14.46
30000	319	335	288	288	9.72	14.03
Mean error					9.89	14.81

It is observed from Table 17 that the maximum deviation of error percentage for the stress above magnet is 0.24 and that for the peak stress is 0.83. This trend implies that even though an error percentage above 10 % exist between the Matlab and FEA resulst, the error is consistent in nature. This helps to calculate a single correction factor that can be adopted in the Matlab code for varying parameters.

4.6 Geometry test on interior permanent magnet

In IPM structure, magnets are buried inside the iron core. This PM structure requires no separate laminations and the obligation of enclosure is also irrelevant here. The complexity in constructing an analytical model for stress calculation of this structure leads to the adoption of a substitute structure that makes the calculation much easier. An equivalent ring replaces the original geometry such that the proposed ring has the same mass density as that of the combined mass density of buried magnets, the thin iron bridge above the magnets and the iron bridge between adjacent magnets which is described in section 3.3. As in the case of SPM, the most prominent stress component in IPM is also the tangential stress. Therefore, the Matlab code limits to the calculation of maximum tangential stress. The basic concept of equivalent ring proposed in [29] is modified by replacing average radius with centroid radius in the calculations of equivalent ring density. The modified equations are used in the Matlab code to find the maximum tangential stress.

The slots for PMs can be customized to reduce the peak stress. There are two alternate methods reviewed in this thesis work to reduce the peak stress. The first one is by providing fillets of same radius at four corners of magnets and the magnet slots. The second method is to provide a semicircular cut at the end of magnet slot. The diameter of the semicircular cut is same as that of the breadth of the magnet slot. This design refrains the geometry from having corner points which accumulate stress. The latter method is followed in this study. Rotational velocity is the only load applied to the model. The Matlab code calculates the maximum tangential stress based on the geometry and rotational velocity. But, the code cannot predict the peak stress which occurs at the corner faces of magnet slot. A correction factor is adopted to calculate the peak stress from the maximum tangential stress calculated by the Matlab code.

Interior permanent magnets buried in a tangential direction inside the rotor core is studied in this section for three different geometries. The outer diameter of rotor and the width of the magnet is varied in each case keeping the rotational speed constant at 15000 rpm. It is observed from similar studies on IPM structure that the maximum tangential stress occurs at the corners of magnet slot in the rotor core [34,35]. This is the peak stress which is impacted by the centrifugal forces and the geometry of the structure. The geometrical impact on the peak stress is accounted by introducing a correction factor based on the results of FE analysis which is discussed in chapter 5. The material data used in the study is given in Table 18. NdFeB is used as the magnet material which is found to be very efficient for IPM structures.[36]

Table 18. Material data for geometry test of IPM

Material Property	Iron Core	PM (NdFeB)
Density (kg/m^3)	7850	7400
Elastic Modulus (GPa)	210	160
Poissons Ratio	0.3	0.24
CTE ($*10^{-6}$) (/°C)	12	8
Yield Strength (MPa)	350	120

Even though an 8 pole IPM is studied, it is assumed that it is sufficient to model a single pole in FE study due to the symmetry of the structure. The FE model details are given in Table 19.

Table 19. FEA model details for geometry test of IPM

Magnet Configuration	8 pole
Magnet slot shape	Rectangular with semicircular edges on short length
Mesh Type	Proximity and Curvature
Mesh size	Medium
Core-Magnet contact type	Frictional (0.2)

The mesh density and stress distribution can be observed from Figure 23. The figure shows three geometrical configurations on the left as listed in Table 20 and the peak stress formation on the right.

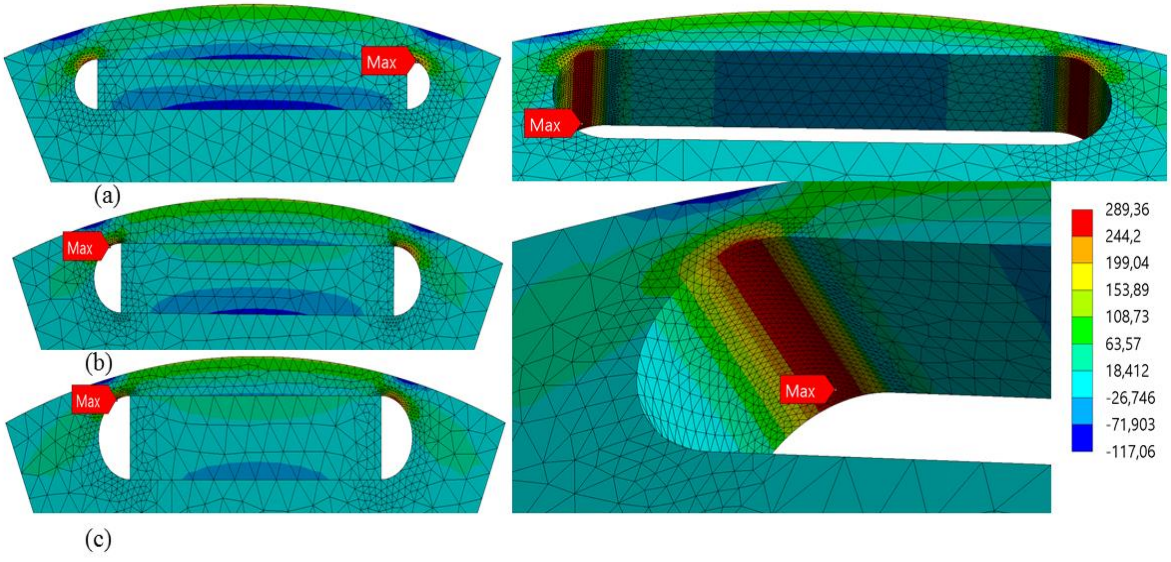

Figure 23. Tangential stress plots in Ansys for IPM geometry test.

The results obtained from Matlab code and the corresponding FE test for similar geometry and load are compared in Table 20. The final column of the table lists the error on comparison between the two methods.

Table 20. Error analysis of IPM geometry test

Rotor outer diameter (mm)	Length of magnet (mm)	Width of magnet (mm)	FEA Stress (MPa)	Matlab Stress (MPa)	Error (%)
84	20	3	155.23	70.26	54.74
94	20	4	204.02	104.64	48.71
104	20	5	289.36	148.44	48.70
Mean Error percentage					50.72

It can be observed from Table 20 that the error percentage is quite high. It is because of the negligence of stress concentration factor in the Matlab code used. A correction factor is calculated based on the results of IPM speed test detailed in the next section. The corrected results are presented in chapter 5.

4.7 Speed test on interior permanent magnet

The third geometry from the geometry test is chosen to perform the speed test in IPM. The material data used for the speed test of IPM is same as that of geometry test and hence it can be referred from Table 18. The dimensions of components for the speed test of IPM is given in Table 21. The magnet is modelled as a 20x5 rectangular bar with no fillets at the corners.

Table 21. Dimensions of components for speed test of IPM

Geometry	Iron Core	PM (NdFeB)
Inner Radius (mm)	0	NA
Outer Radius (mm)	52	NA
Length (mm)	NA	20
Breadth (mm)	NA	5
Height of iron bridge above magnets (mm)	2	

Table 22 lists the general parameters used in the speed test of IPM structure. Rotational velocity is varied from 10000 to 30000 rpm with an increment of 5000 rpm at each successive test. Thermal gradient between the rotor assembly and the outside environment is neglected in this study.

Table 22. General parameters for speed test of IPM

Rotational velocity (rpm)	10000-30000
Thermal gradient (℃)	0

One segment of the 8 pole IPM is modelled in Ansys to study the peak stress under rotational load. The contact between magnet and the iron core is modelled as frictional providing a friction coefficient of 0.2. Table 19 lists the FEA data used for the study.

The meshing details can be observed from Figure 24 where fine meshing is provided in the corners of the magnet slot where stress peaks are expected. The meshing is refined until a point where the results converge such that an increase in mesh density no longer has an impact on the results. Figure 24 demonstrates the occurrence of peak stress in the magnet slot corners. The maximum stress is selected for comparison with Matlab results.

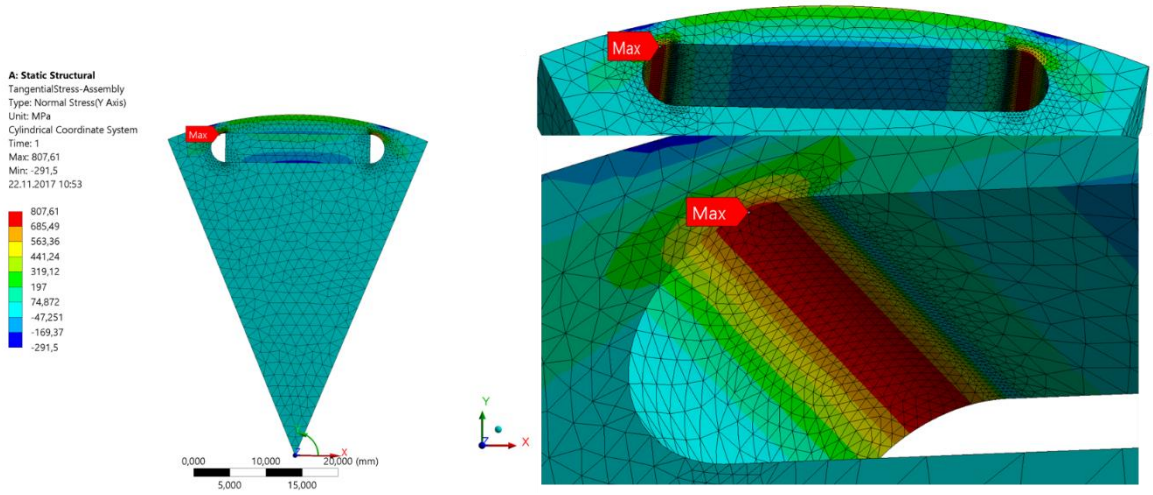

Figure 24. Tangential stress plot in Ansys for IPM speed test

Table 23 tabulates the Matlab results and compares the corresponding values to the FEA peak stress. The comparison is presented in the form of error analysis detailing the deviation of Matlab peak stress from FEA peak stress.

Table 23. Error analysis of IPM speed test

RPM	Fe Stress (MPa)	Matlab Stress (MPa)	Error (%)
10000	91.66	46.5	49.27
15000	204.02	104.64	48.71
20000	359.24	186.03	48.22
25000	561.05	290.68	48.19
30000	807.61	418.57	48.17
Mean Error			48.51

It is evident from the error analysis that the error percentage decrease slightly with the increase in speed. This might be because the method adopted is based on centrifugal force which is directly proportional to the square of velocity and the speed predominates geometry at higher rpm. It can be inferred from this analysis that the difference between maximum and minimum error percentage is only 1.1%. The method adopted is useful to find the peak stress by applying a correction factor but does not guarantee high level of accuracy. Hence, further refinement of the equivalent ring approach is advisable for future studies.

4.8 Geometry test on V-shaped permanent magnet

VPM is an alternate form of IPM where the buried magnets form a magnet pair with V shape. The angle between the magnet pair is a variable. V magnets coincide with the IPM structure studied in the previous section when the angle between the magnet pair approaches 180 degree. The angle used in this study is 150 degree. An equivalent ring approach, similar to the one used in IPM study is also used here. Apart from transferring the density of magnet and iron bridge to the equivalent ring, the centroid radius of the proposed ring is also calculated based on the centroids of different sections of the original VPM structure. The transfer of centroid provides more accuracy to stress calculation of VPM since the centroid varies with the angle between the magnet pair.

The magnet pair in VPM can be arranged in various fashion. The space between the pair of magnets is designed to optimize both the mechanical as well as electromagnetic performance. Thinner bridges reduce leakage flux, whereas thick bridge between the magnets enhance mechanical performance [34,37]. Different designs are proposed by various authors to optimize these contradicting constraints. In this study, mechanical

performance is given importance. Hence, the space between magnet pairs is mostly occupied by the rotor iron except for a tiny air gap passage connecting the slots of magnet pairs. The material data for VPM geometry test is given in Table 24.

Table 24. Material data for VPM geometry test

Material Property	Iron Core (S350)	PM (NdFeB)
Density(kg/m^3)	7850	7400
Elastic Modulus (GPa)	210	160
Poissons Ratio	0.3	0.24
CTE ($*10^{-6}$) (/°C)	12	8
Yield Strength (MPa)	350	120

Three different geometries studied are listed in Table 25 where the outer diameter of rotor core and the width of the magnet are varied while keeping the speed of the rotor constant at 15000 rpm. Table 25 compares the Matlab and FE analysis results to calculate the error percentage of results obtained from Matlab code.

Table 25. Error analysis of VPM geometry test

Rotor outer diameter (mm)	Length of magnet (mm)	Width of magnet (mm)	FEA Stress (MPa)	Matlab Stress (MPa)	Error (%)
84	20	3	247.82	74.74	69.84
94	20	4	320.18	100.58	68.59
104	20	5	417.57	131.58	68.49
Mean Error percentage					68.97

It can be concluded from the error analysis of VPM that the error percentage is rather high but consistent in nature. It can be inferred from the result that the tangential stress calculation failed to calculate the peak stress due to geometric discontinuities. This is accounted in the form of a correction factor discussed in chapter 5.

4.9 Speed test on V-shaped permanent magnet

The third geometry from Table 25 is selected to do a speed test with rotational velocities ranging from 10000 to 30000 rpm. Thermal gradient is ignored in this study. The material used is same as that used in geometry test and hence can be referred from Table 24.The dimensions used to model iron core and the magnets is listed in Table 26.

Table 26. Dimensions of components for the speed test of VPM

Geometria data	Iron Core	PM (NdFeB)
Inner Radius (mm)	0	NA
Outer Radius (mm)	52	NA
Length(mm)	NA	20
Breadth(mm)	NA	5
Height of iron bridge above magnets(mm)	2	
Angle between magnets of a single pole (deg)	150	
Pole angle (deg)	60	

An Ansys model is created using the same material and geometric data as referred from Table 24 and Table 26 respectively. In order to reduce the stress peaks, fillets of same radius are provided at the four corners of the magnets and the magnet slots. A 60 degree section of 6 pole VPM structure is modelled in Ansys with 150 degree angle between the magnet pair. The data used to create Ansys model for VPM structure is provided in Table 27.

Table 27. FEA model details for the speed test of VPM

Magnet Configuration	6 pole
Magnet slot shape	Rectangular, fillets at 4 corners
Mesh Type	Proximity and Curvature
Mesh size	Medium
Core-Magnet contact type	Frictional (0.2)

The mesh density and mesh distribution are illustrated in Figure 25 in which a finer mesh is provided at the top corners of magnet slots where the peak stress is expected.

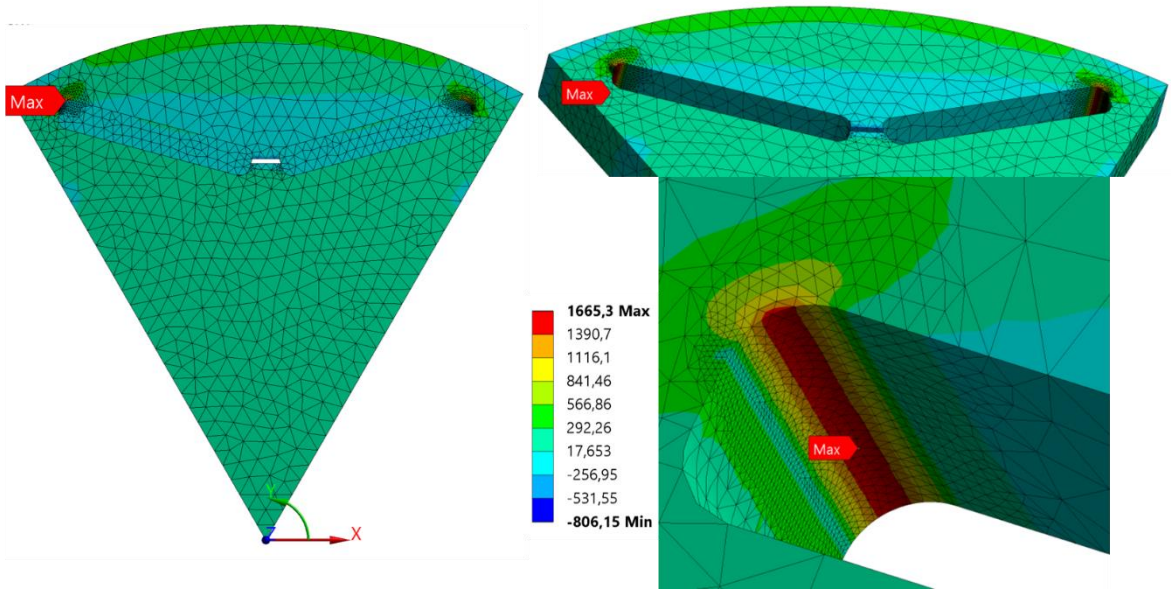

Figure 25. Tangential stress plot in Ansys for VPM speed test

Stress peaks in VPM can occur at two different points, one at the bilateral iron bridge above the magnets and the other one at the central bridge between magnet pair . It is observed under repeated experiments that the peak stress occurs always at the central bridge and specifically at the corners of the magnet slot.

The analytical stress calculation at the central bridge and bilateral bridge of VPM require different approaches. Since the peak stress always occurs in the bilateral bridge, the Matlab code focus on finding the maximum stress at the bilateral bridge. But, the code calculates only the maximum tangential stress which does not coincide with the peak stress. Peak stress is dependent on the details of geometry like the ratio of dimensions and radius of fillets used. There are different mathematical approaches to find the SCF which can predict the peak stress. But the approach used here is to derive a SCF based on successive speed tests on the same geometry. The SCF calculation is detailed in analysis section. Table 28 presents the error analysis of VPM speed test which compares results from Matlab code with the corresponding FEA results.

Table 28. Error analysis of VPM speed test

RPM	Fe Stress (MPa)	Matlab Stress (MPa)	Error (%)
10000	186.7	58.48	68.68
15000	417.57	131.58	68.49
20000	739.5	233.92	68.37
25000	1153.6	365.5	68.32
30000	1665.3	526.32	68.39
Mean Error			68.45

It is clearly evident form the error analysis of VPM speed test as seen in Table 28 that the error percentage at different speed maintains good consistency such that the maximum deviation from mean error is 0.36% which is quite low. Despite the fact that the error percentage is quite big, it assures reliability due to small error tolerance across the range of experiments. The high percentage in error is explained by the fact that the peak stress in Ansys model is compared against the maximum tangential stress in Matlab and not against the peak tangential stress. The error percentage from Table 28 is utilized to find the SCF which is then used to find the peak stress in Matlab. The comparison between the corrected Matlab results and FEA peak stress is presented in the analysis section where the error percentage is reduced considerably to obtain fairly accurate result.

5 ANALYSIS

A detailed analysis of the results is carried out in this section to study the accuracy of the obtained result. The results are first reviewed graphically and then a correction factor is calculated based on the data of speed test for the four different magnet types. It is important to note that even though error percentage in a certain group of experiments is high, it is possible to derive a reliable correction factor if the errors are consistent in nature. In case of inconsistent errors resulting from scattered data, it is not possible to find a CF that suits entire range of data. The CF is first applied in the same speed test results which are used to derive the CF to portray the possible reduction in error percentage. Next, the reliability of CF is ensured by using the same CF in the geometry test for all the four different methods studied in this thesis. Error analysis of the four methods are represented graphically in Figure 26.

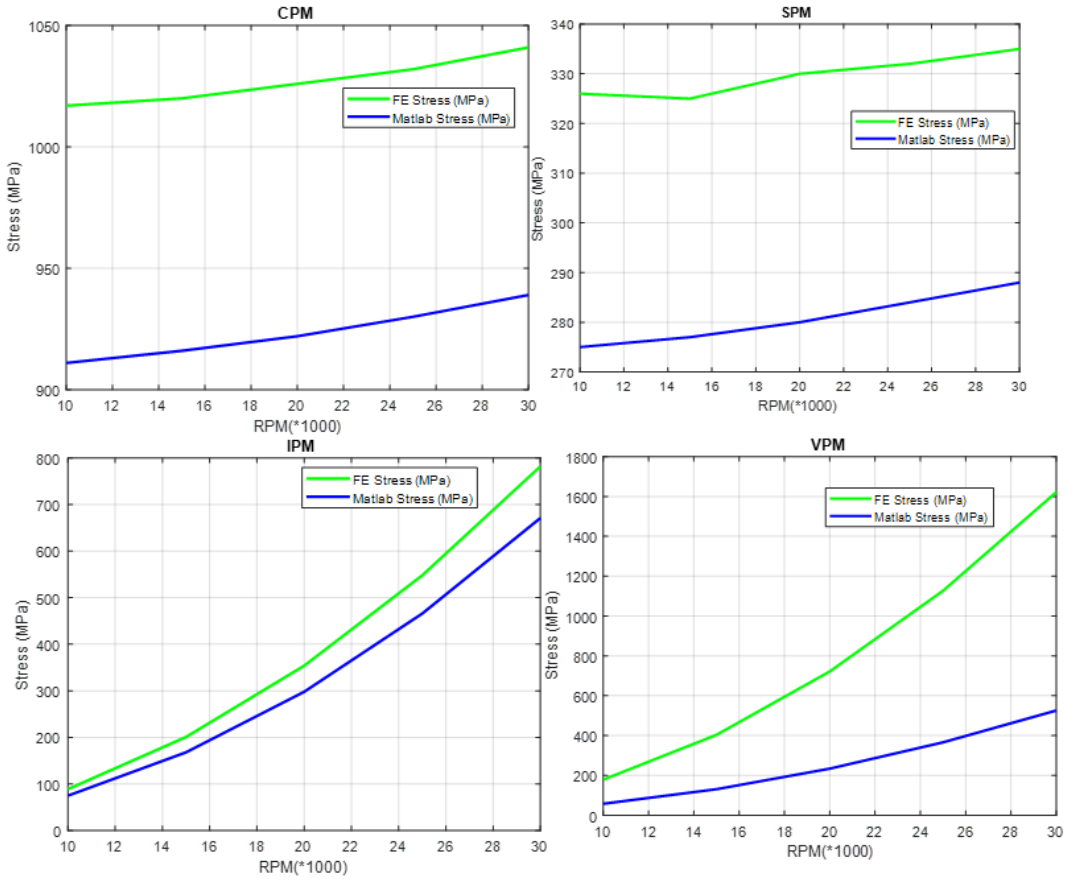

Figure 26. Graphical representation of error analysis of the four methods CPM, SPM, VPM and IPM in clockwise direction.

As stated previously, a correction factor is introduced to minimize the error whose calculation is presented by equation(64). The speed tests are only considered for this calculation.

$$CF = \frac{\sum \text{Fe stress} + \sum Matlab\ stress}{n} \quad (64)$$

Where n denotes the number of experiments taken into account for CF calculation. Here, 5 experiments are conducted and all of them are considered to calculate the CF which gives n a value of 5. The summation of FEA and Matlab stress are obtained from Table 11, Table 17, Table 23 and Table 28. Table 29 presents the CF calculated for the four different methods CPM, SPM, IPM and VPM.

Table 29. Correction factor calculation for four independent methods

Method	∑Fe Stress (MPa)	∑Matlab Stress (MPa)	CF
CPM	1041	939	1.11
SPM	1650	1404	1.18
IPM	2024	1046	1.93
VPM	3976	1257	3.16

The correction factors from Table 29 are used in the respective Matlab code to get corrected Matlab results. Table 30 presents the error analysis of CPM speed test in which a CF of 1.11 is used to correct the maximum tangential stress.

Table 30. Error analysis of CPM speed test in which Matlab results are corrected with a CF of 1.11

RPM	Fe Stress (MPa)	Matlab Stress (MPa)	Error (%)
10000	1017	1011	0.59
15000	1020	1017	0.29
20000	1026	1023	0.29
25000	1032	1032	0.00
30000	1041	1042	0.10
Mean error			0.25

It is evident from Table 11 and Table 30 that the mean error percentage of the 5 experiments reduced from 10.09 to 0.25 while applying the CF. The same CF is applied in the CPM geometry test as well to correct the Matlab results of maximum tangential stress. The corrected results are presented in Table 31.

Table 31. Error analysis of CPM geometry test in which Matlab results are corrected with a CF of 1.11

Enclosure Diameter (mm)	FEA Stress (MPa)	Matlab Stress (MPa)	Error (%)
85	1130	1127	0.27
95	1020	1017	0.29
105	929	928	0.11
Mean Error			0.22

It can be seen from Table 31 that the Matlab results corrected with same CF gives fairly accurate results for CPM geometry test as well which ensures the reliability of selected CF and the method adopted to calculate the CF. Table 32 presents the error analysis of SPM speed test.

Table 32. Error analysis of SPM speed test in which peak stress in Matlab results are corrected with a CF of 1.18

RPM	FEA		Corrected Matlab Results		Error %	
	Stress above magnet (Mpa)	Peak stress (MPa)	Stress above magnet (MPa) (CF=1.11)	Peak stress (MPa) (CF=1.18)	Stress above magnet (%)	Peak stress (%)
10000	306	326	305.25	324.5	0.25	0.46
15000	308	327	307.47	326.86	0.17	0.04
20000	311	330	310.8	330.4	0.06	0.12
25000	314	332	315.24	335.12	0.39	0.94
30000	319	335	319.68	339.84	0.21	1.44
Mean error					0.22	0.60

A CF of 1.11 is used in the Matlab code to calculate the stress above magnet. A separate CF of 1.18 is used to predict the peak stress which occurs above the separation material. It is obvious by comparing Table 17 and Table 32 that the mean error in the calculation of stress above magnet reduced from 9.89 to 0.22. Meanwhile, peak stress of 5 successive speed test reduced from 14.91 to 0.6 by using the CF. The prediction of stress above magnet looks more reliable due to better distribution of individual error percentages around the mean value. Now, the same CF used in SPM speed test is applied for SPM geometry test and the corrected results are presented in Table 33.

Table 33. Error analysis of SPM geometry test in which peak stress in Matlab results are corrected with a CF of 1.18

Enclosure Diameter (mm)	Fe Stress (MPa)		Matlab Stress (MPa)		Error %	
	Stress above magnet	Peak stress	Stress above magnet (CF=1.11)	Peak stress (CF=1.17)	Stress above magnet	Peak stress
85	308	327	307.47	326.86	0.17	0.04
95	278	293	275.28	292.64	0.98	0.12
105	253	264	250.86	266.68	0.85	1.02
Mean error					0.67	0.39

It can be seen from Table 33 that the error percentage does not go above 1% when the CF derived from SPM speed test is applied to the geometry test. And hence, this correction factor can be used in the Matlab code to correct the calculated tangential stress for different geometries as well.

Table 34 presents the error analysis of IPM speed test in which a CF of 1.93 is used in the Matlab code to calculate the maximum tangential stress that occurs at the bilateral bridge above magnets.

Table 34. Error analysis of IPM speed test in which Matlab results are corrected with a CF of 1.93

RPM	Fe Stress (MPa)	Matlab Stress (MPa)	Error
10000	91.66	89.75	2.08
15000	204.02	201.96	1.01
20000	359.24	359.04	0.06
25000	561.05	561.01	0.01
30000	807.61	807.84	0.03
Mean Error			0.64

The mean error percentage of IPM speed test reduced from 48.51 to 0.64 by using a CF. It can also be seen from Table 34 that the applied CF well suits higher rotational speed than lower ones. Since the error percentage rise above 2% for the first rotational speed of 10000 rpm, it can be concluded that reliability of CF for the data range of lower speeds is low.

The same CF which was used in SPM speed test is now applied to SPM geometry test and the results are presented in Table 35.

Table 35. Error analysis of IPM geometry test in which Matlab results are corrected with a CF of 1.93

Rotor outer diameter (mm)	FEA Stress (MPa)	Matlab Stress (MPa)	Error (%)
84	155.23	135.6	12.65
94	204.02	201.96	1.01
104	289.36	286.49	0.99
Mean Error			4.88

It can be seen form Table 35 that the error percentage has reduced considerably for the second and third geometry studied. But the error percentage of the first geometry which is 12.65 is not acceptable. Hence, it can be concluded that the estimated CF is not applicable for low diameter rotors.

Table 36 presents the error analysis of IPM speed test in which a CF of 3.16 is used in the Matlab code to calculate the maximum tangential stress.

Table 36. Error analysis of VPM speed test in which Matlab results are corrected with a CF of 3.16

RPM	Fe Stress (MPa)	Matlab Stress (MPa)	Error (%)
10000	186.7	184.80	1.02
15000	417.57	415.79	0.43
20000	739.5	739.19	0.04
25000	1153.6	1154.98	0.12
30000	1665.3	1663.17	0.13
Mean Error			0.35

Even though the CF used in VPM speed test is quite high, the results obtained looks quite reliable. The mean error percentage reduced from 68.45 to 0.35. The use of a large CF is reasonable since the Matlab code does not use analytical approach to calculate the SCF. Instead this particular method relies on error analysis based on Ansys results to determine the CF which is then used as the SCF in this scenario. The same CF is now applied to VPM geometry test and the results are tabulated in Table 37.

Table 37. Error analysis of VPM speed test in which Matlab results are corrected with a CF of 3.16

Rotor outer diameter (mm)	FEA Stress (MPa)	Matlab Stress (MPa)	Error (%)
84	247.82	236.18	4.70
94	320.18	317.83	0.73
104	417.57	415.79	0.43
Mean Error			1.95

It can be inferred from Table 37 that the CF applies quite well for larger diameter rotors and the error percentage reduces as the size of rotor increases. Even though, the error percentage for the first geometry looks quite high, the CF can still be used for different geometries since none of the error percentage rise above 5%.

6 DISCUSSION

The previous section presented the Matlab results based on the code developed in this study for four different PM rotors. Afterwards, the same geometry was built in Ansys and it was considered as the reference model to compare the Matlab results obtained. The error percentage between the two methods were analyzed in the previous section. This chapter reviews the reason behind the possible errors and suggest improved methods based on the knowledge acquired during the course of this thesis study which would help to continue this work in a more effective manner with comparatively less error percentage. Additionally, a review on sensitivity, accuracy, reliability and validity analysis of this thesis work is done at the end of this section

A brief review of the results and analysis section shows that the error percentage in the first two PM rotors CPM and SPM were low and the results were quite consistent. Hence, these results can be concluded as reliable ones. Meanwhile, as clearly stated in the limitations of the thesis work, certain parameters like the variation of CTE, isotropic behavior of materials, momentum considerations of rotor are neglected in the study. The developed code can be reused by incorporating all these aspects to obtain a result closer to reality.

It can be observed by reviewing the results and analysis of IPM rotor that the results of speed test are consistent while the error percentage is quite high. Even though the calculated CF works well for the speed test, it gives an error of 12.65 % for the smallest geometry when the same CF is applied to the geometry test. This implies that the proposed equivalent ring approach is not quite reliable to be used across varying geometries, especially for rotors with small diameters. Two suggestions are proposed here to eliminate this error. The most reliable option would be to use the partial differential toolbox for structural mechanics in Matlab to define the geometry of the PM rotor with better precision. This tool allows user to create 2D or 3D models using a procedure similar to that adopted in finite element based tools like Ansys. The procedure followed involves the creation of geometry, meshing of geometry, applying constraints or boundary conditions and obtaining the results. This similarity in techniques adopted in Matlab can provide results closer to that given by Ansys. But a compromise has to be made in terms of computational speed. Firstly, there are two methods

by which a geometry can be introduced. It can either be imported from a CAD (computer aided design) based software or can be built in Matlab by using a function called CSD (constructive solid geometry) which allow user to create 2D geometry using basic building blocks such as circle, square, rectangle etc. Creation and importing of 3D model is time consuming whereas CSD is not suitable for complex geometries. Even though this approach reduces the errors accumulated due to the consideration of equivalent ring, it is more time consuming. Hence the choice purely depends on the requirement of accuracy and constraints on development time of the model. The second suggestion is to calculate the stress concentration factors mathematically in order to accommodate factors such as fillet radius ratio. Additionally, the tangential stress formula can be improvised by adding more geometrical parameters like bridge thickness ratio, magnet depth ratio, magnet thickness ratio and web ratio to get more accurate results.

The stress analysis of VPM rotors looks more reliable than the IPM results despite the fact that an equivalent ring approach is used in this case as well. Even though the error percentage is quite high, the calculated CF reduces the error percentage considerably in speed test as well as in geometry test. Hence, it can be inferred that the calculated CF is applicable to different speeds and for varying geometries of VPM.

6.1 Sensitivity analysis

The sensitivity of the developed Matlab code in predicting the maximum stress under varying input parameters is measured by conducting mainly two different types of test runs; the speed test and geometry test. The speed of a particular geometry is varied 5 times in speed test and the geometry is varied thrice by keeping the speed constant in geometry test. This procedure ensures that the changing input parameters doesn’t drastically affect the stress prediction made by Matlab code.

6.2 Accuracy analysis

Accuracy analysis of this thesis coincides with the error analysis where the Matlab results are compared against Ansys results to calculate the percentage in error. The accuracy in Matlab code prediction is determined by this comparison which is adopted throughout all the test runs in this thesis work.

6.3 Reliability analysis

The reliability of the developed code to be used in different type of rotor configurations and different speed ranges is ensured by deriving a CF based on speed test and using the same CF in geometry test. This ensures that the code and CF are not specific to certain parameters used in the code but can be applied across different geometries and speed variations.

6.4 Validity analysis

Since Ansys models are used as the reference source for accuracy analysis, the validity of the adopted procedure is certified by ensuring that the stress pattern obtained concurs with the conclusions derived in the literature review. The stress distribution and variation in CPM agrees with the works of previous authors for radial and tangential stress. As seen from the literature, the peak stress in SPM occurs in the enclosure region above filler material. In case of IPM, as reviewed in the literature, the peak stress was observed in the corner faces of magnet slots. Similarly, the IPM test results also concur with the literature study where the peak stress occurs in the bilateral bridge.

7 CONCLUSION

This thesis is presented based on the bearingless project at Lappeenranta University of Technology which aims at commercializing the bearingless drives. As a part of this project, analytical tool to calculate initial mechanical stress in four different PM rotors is developed in this study. The four PM rotors studied are CPM, SPM, IPM and VPM. The analytical tool is developed in Matlab 17 and verified in Ansys 18.

The thesis is realized in five consecutive phases. In the first phase, the parametric tool is developed in Matlab based on the analytical formulations of four PM rotors studied in literature. In order to derive the analytical solution, firstly the basic equations for radial and tangential stress for a rotating cylinder is derived under centrifugal load. Boundary conditions of a three layer shrink fitted structure is applied to these equations to get the analytical solution of first and the most basic PM rotor which is CPM. The same principle is used in SPM as well since the section of SPM including the iron core, magnet and enclosure resembles the section of CPM. However, the peak stress of SPM occurs in the enclosure above the filler material separating the two adjacent magnets. This peak stress is found by applying a SCF to the maximum tangential stress in the enclosure above the magnet. The SCF is determined from the peak stress in the corresponding Ansys models. An equivalent ring approach is followed to find the maximum tangential stress in IPM structure. The equivalent ring is defined such that its density is equivalent to the combined density of magnet and surrounding iron bridge and the centrifugal forces acting on equivalent ring is equal to the centrifugal forces acting on original structure. A similar approach is followed to find the maximum tangential stress of VPM structure as well. In a VPM, the peak stress occurs at the bilateral bridge. Therefore, the equivalent ring density is calculated based on the densities and centroid radius of magnet pair and bilateral bridge.

The second phase involves building Ansys models for the four PM rotors based on geometry and material properties already defined in Matlab code during the first phase. The sensitivity of Ansys results is very crucial at this stage because it can negatively impact the prediction of error since Ansys model is used as the reference for comparison. Hence, the Ansys model used for comparison is chosen after multiple trials to converge the solution.

The third phase is the testing phase where Matlab and Ansys results for the same input parameters are compared to find out the error in Matlab code by keeping the corresponding Ansys results as the reference. Three different tests done to compare the results are speed test, geometry test and thermal test. Speed test and geometry tests are done for all the four PM rotor types, while thermal test is done only for the first PM which is CPM. Stress variation at 5 different speeds from 10000 to 30000 rpm is studied in speed test where all other parameters excluding the speed like geometry and material properties are maintained constant. Similarly, three different geometries are studied in geometry test. In thermal test, the presence and absence of thermal gradient is studied.

A correction factor for the analytical tool is calculated in the fourth stage based on the error analysis data from speed test of previous stage. The reliability of this correction factor tested in the final stage where the CF developed form speed test is used in the geometry test to verify the universal nature of the calculated CF.

Of all the 4 different PM rotors studied, the code developed for CPM and SPM gave satisfactory results. The method adopted to calculate maximum tangential stress in IPM requires some revision to accommodate geometrical factors such as fillet radius ratio to predict the peak stress more accurately. VPM test cases gave reliable results in terms of the calculated CF which could reduce the error percentage considerably.

It can thus be concluded that the developed tool is sufficient to calculate the initial stress in high speed rotors for the four PM rotors studied. The approximations considered in the limitations section of this thesis needs to be eliminated completely in order to achieve higher accuracy in results. Moreover, it is suggested to use the partial differential toolbox for structural mechanics in Matlab to define the geometry of IPM and VPM more precisely in order to get results closer to that obtained from FEA.

REFERENCES

[1]Design aspects and test results of a high speed bearingless drive. Power Electronics and Drive Systems (PEDS), 2011 IEEE Ninth International Conference on: IEEE; 2011.

[2]Ooshima M, Kitazawa S, Chiba A, Fukao T, Dorrell D. Design and analyses of a coreless-stator-type bearingless motor/generator for clean energy generation and storage systems. IEEE Trans Magn 2006;42(10):3461-3463.

[3]Chiba A, Fukao T, Ichikawa O, Oshima M, Takemoto M, Dorrell DG. Magnetic bearings and bearingless drives. : Elsevier; 2005.

[4]W. Amrhein, S. Silber, K. Nenninger. Levitation forces in bearingless permanent magnet motors. IEEE Transactions on Magnetics 1999;35(5):4052-4054.

[5]Permanent magnet bearingless motors: Modelling, design and drive. 2017 IEEE Workshop on Electrical Machines Design, Control and Diagnosis (WEMDCD); 2017.

[6]Modeling and Design of Super High Speed Permanent Magnet Synchronous Motor (PMSM). 2008 IEEE National Aerospace and Electronics Conference; 2008.

[7]Rotor design of a high-speed Permanent Magnet Synchronous Machine rating 100,000 rpm at 10kW. 2010 IEEE Energy Conversion Congress and Exposition; 2010.

[8]Schoeb R, Barletta N. Principle and application of a bearingless slice motor. JSME International Journal Series C Mechanical Systems, Machine Elements and Manufacturing 1997;40(4):593-598.

[9]Borisavljevic A. Limits, modeling and design of high-speed permanent magnet machines. : Springer Science & Business Media; 2012.

[10]C. Zwyssig, S. D. Round, J. W. Kolar. An Ultrahigh-Speed, Low Power Electrical Drive System. IEEE Transactions on Industrial Electronics 2008;55(2):577-585.

[11]A. Borisavljevic, H. Polinder, J. A. Ferreira. On the Speed Limits of Permanent-Magnet Machines. IEEE Transactions on Industrial Electronics 2010;57(1):220-227.

[12]Rotor strength analysis for high speed permanent magnet machines. 2014 17th International Conference on Electrical Machines and Systems (ICEMS); 2014.

[13]Chiba A, Power D, Rahman M. Characteristics of a bearingless induction motor. IEEE Trans Magn 1991;27(6):5199-5201.

[14]Salazar AO, Stephan R. A bearingless method for induction machines. IEEE Trans Magn 1993;29(6):2965-2967.

[15]Analysis and design of an ultra-high-speed slotless self-bearing permanent-magnet motor. IECON 2012-38th Annual Conference on IEEE Industrial Electronics Society: IEEE; 2012.

[16]Mitterhofer H, Gruber W, Amrhein W. On the high speed capacity of bearingless drives. IEEE Trans Ind Electron 2014;61(6):3119-3126.

[17]S. J. Galioto, P. B. Reddy, A. M. EL-Refaie, J. P. Alexander. Effect of Magnet Types on Performance of High-Speed Spoke Interior-Permanent-Magnet Machines Designed for Traction Applications. IEEE Transactions on Industry Applications 2015;51(3):2148-2160.

[18]A design consideration of a novel bearingless disk motor for artificial hearts. Energy Conversion Congress and Exposition, 2009. ECCE 2009. IEEE: IEEE; 2009.

[19]Yang S, Huang M. Design and implementation of a magnetically levitated single-axis controlled axial blood pump. IEEE Trans Ind Electron 2009;56(6):2213-2219.

[20]Comparison of winding concepts for bearingless pumps. Power Electronics, 2007. ICPE'07. 7th Internatonal Conference on: IEEE; 2007.

[21]Masuzawa T, Kita T, Okada Y. An ultradurable and compact rotary blood pump with a magnetically suspended impeller in the radial direction. Artif Organs 2001;25(5):395-399.

[22]Reichert T, Nussbaumer T, Kolar JW. Bearingless 300-W PMSM for bioreactor mixing. IEEE Trans Ind Electron 2012;59(3):1376-1388.

[23]Warberger B, Kaelin R, Nussbaumer T, Kolar JW. 50-N.m/2500-W Bearingless Motor for High-Purity Pharmaceutical Mixing. IEEE Trans Ind Electron 2012;59(5):2236-2247.

[24]Hearn EJ. Mechanics of Materials 2: The mechanics of elastic and plastic deformation of solids and structural materials. : Butterworth-Heinemann; 1997.

[25]Rene Larsonneur. Design and Control of Active Magnetic Bearing Systems for High Speed RotationSwiss Federal Institute of Technology; 1990.

[26]Zhang F, Du G, Wang T, Liu G, Cao W. Rotor retaining sleeve design for a 1.12-MW high-speed PM machine. IEEE Trans Ind Appl 2015;51(5):3675-3685.

[27]Mechanical design method for a high-speed surface permanent magnet rotor. Energy Conversion Congress and Exposition (ECCE), 2016 IEEE: IEEE; 2016.

[28]Mechanical design of outer-rotor structure for dual mechanical port machine. Electrical Machines and Systems (ICEMS), 2011 International Conference on: IEEE; 2011.

[29]A. Binder, T. Schneider, M. Klohr. Fixation of buried and surface-mounted magnets in high-speed permanent-magnet synchronous machines. IEEE Transactions on Industry Applications 2006;42(4):1031-1037.

[30]Jung J, Lee B, Kim D, Hong J, Kim J, Jeon S, et al. Mechanical stress reduction of rotor core of interior permanent magnet synchronous motor. IEEE Trans Magn 2012;48(2):911-914.

[31]Varaticeanu BD, Minciunescu P, Fodorean D. Mechanical design and analysis of a permanent magnet rotors used in high-speed synchronous motor. Electrotehnica, Electronica, Automatica 2014;62(1):9.

[32]Jong IC, Rogers BG. Engineering Mechanics: Statics. : Oxford University Press; 1995.

[33]Chai F, Li Y, Liang P, Pei Y. Calculation of the maximum mechanical stress on the rotor of interior permanent-magnet synchronous motors. IEEE Trans Ind Electron 2016;63(6):3420-3432.

[34]Bridge stresses and design in IPM machines. EUROCON 2009, EUROCON'09. IEEE: IEEE; 2009.

[35]Analysis of the rotor mechanical strength of interior permanent magnet synchronous in-wheel motor with high speed and large torque. Transportation Electrification Asia-Pacific (ITEC Asia-Pacific), 2014 IEEE Conference and Expo: IEEE; 2014.

[36]Rahman MA. History of interior permanent magnet motors [History]. IEEE Ind Appl Mag 2013;19(1):10-15.

[37]Lim D, Yi K, Woo D, Yeo H, Ro J, Lee C, et al. Analysis and design of a multi-layered and multi-segmented interior permanent magnet motor by using an analytic method. IEEE Trans Magn 2014;50(6):1-8.

APPENDIX

APPENDIX I : Matlab code that plots radial, tangential and von Mises stress in CPM

```
RADIAL AND TANGENTIAL STRESS CALCULATION FOR CYLINDRICAL PERMANENT MAGNET
%All values are given in SI units
%lITERATURE-Mechanics of Materials 2: The mechanics of elastic and plastic
%deformation of solids and structural materials(Hearn, Edwin John)
%Created by: Devika Sasi
%Date: 28.11.2017

clear all;
close all
clc;
format long
tic;

%############CONSTANTS DEFINITION############
Steps = 300; %  Number of simulation stepss
FS = 2; % factor of safety
delta_T = 0; % temperature difference
delta_r = 100e-6; %radial interference
rpm_min=0;%Minimum rpm
rpm_max = 15000;%Maximum rpm
ohmega = rpm_max/60*2*pi;%Angular velocity
% ###################################################

%############MATERIAL DATA############

%Material_1-steelS355
sigma_y1=335e6; %Yield strength(for diameter between 40 and 60 mm)
E1=210e9;%Elastic modulus
v1=0.3;%Poisson ratio
rho1=7850;%Density
alpha1 = 12.6e-6; %Coefficient of tehrmal expansion

%Material_2-Magnet(Cobalt Iron)
sigma_y2=220e6;%annealed for optimum magnetic properties
E2=230e9;
v2=0.29;
rho2=8600;
alpha2 = 12e-6; % Coef. of therm. expansion
%Material_3-Carbonfiber(general data and not accurate values)
sigma_y3=600e6;
E3=228e9;
v3=0.320;
rho3=1800;
alpha3 = 13e-6; % Coef. of therm. expansion
%########################################

%############GEOMETRY(in SI units)##################

rfei = 0e-3;
rfeo = 35.5e-3 + alpha1*delta_T*(35.5e-3);


rmi = 35.5e-3 -delta_r + alpha2*delta_T*(35.5e-3);
rmo =40.5e-3+ alpha2*delta_T*(40.5e-3);

reo = 40.5e-3 -delta_r + alpha3*delta_T*(40.5e-3);
reo =42.5e-3+ alpha3*delta_T*(42.5e-3);
%#####################################

%####Integration Constants################

syms a b  a1_ b1_ a2_ b2_ a3_ b3_ r_ v  rho  E  sigma_r sigma_t

u = (a * r_) + b/r_ - (1 -v^2) * (rho * r_^3 * ohmega^2)/(8*E);%Displacement Equation [REFER
EQUATION (24)]
```

```
epsr = diff(u,'r_')% Radial strain Equation 1 [REFER EQUATION (18)]
epst = u/r_% Tangential strain Equation 1 [REFER EQUATION (19)]

epsr_ = 1/E * (sigma_r - v * sigma_t);% Radial strain Equation 2 [REFER EQUATION (21)]
epst_ = 1/E * (sigma_t - v * sigma_r);% Tangential strain Equation 2 [REFER EQUATION (22)]


res1 = epsr - epsr_;
res2 = epst - epst_;

sigma_t_ = solve(res2, sigma_t)%Tangential stress

res3 = subs(res1,sigma_t,sigma_t_);

res4 = res3 == 0

sigma_r_= isolate(res4,sigma_r)%Radial Stress

%#################Stress&Displacement Equations#############################

sigma_rfeo=subs(rhs(sigma_r_),[r_,a,b,E,v,rho],[rfeo,a1_,b1_,E1,v1,rho1]);
sigma_rmi=subs(rhs(sigma_r_),[r_,a,b,E,v,rho],[rmi,a2_,b2_,E2,v2,rho2]);
u_rfeo=subs(u,[r_,a,b,E,v,rho],[rfeo,a1_,b1_,E1,v1,rho1]);
u_rmi= subs(u,[r_,a,b,E,v,rho],[rmi,a2_,b2_,E2,v2,rho2]);
sigma_rmo=subs(rhs(sigma_r_),[r_,a,b,E,v,rho],[rmo,a2_,b2_,E2,v2,rho2]);
sigma_reo=subs(rhs(sigma_r_),[r_,a,b,E,v,rho],[reo,a3_,b3_,E3,v3,rho3]);
u_rmo=subs(u,[r_,a,b,E,v,rho],[rmo,a2_,b2_,E2,v2,rho2]);
u_reo= subs(u,[r_,a,b,E,v,rho],[reo,a3_,b3_,E3,v3,rho3])
sigma_reo=subs(rhs(sigma_r_),[r_,a,b,E,v,rho],[reo,a3_,b3_,E3,v3,rho3]);
%#########################################################################

%######################BOUNDARY CONDITIONS################################
bound_1=b1_==0;
bound_2=sigma_rfeo==sigma_rmi;
bound_3=rfeo+u_rfeo==rmi+u_rmi;
bound_4=sigma_rmo==sigma_reo;
bound_5=rmo+u_rmo==reo+u_reo;
bound_6=sigma_reo==0;
%#########################################################################

%######################SOLUTION###########################################
sol=solve([bound_1,bound_2,bound_3,bound_4,bound_5,bound_6],[a1_,a2_,a3_,b1_,b2_,b3_]);
a1=sol.a1_;
a2=sol.a2_;
a3=sol.a3_;
b1=sol.b1_;
b2=sol.b2_;
b3=sol.b3_;

x=double([a1 b1 a2 b2 a3 b3]')


%#########################################################################
r = linspace(rfei+50e-6,reo,Steps);%Radius
u = zeros(Steps,1);%Dispalcement
epsilon_r = zeros(Steps,1);%Radial strain
epsilon_t = zeros(Steps,1);%Tangential strain
sigma_ref_max = zeros(Steps,1);%Reference stress


    for m = 1:Steps % Radius loop
        if r(m) <= rfeo
            u(m) = x(1)*r(m) + x(2)/r(m) - (1-v1^2)/8/E1*rho1*r(m)^3*ohmega^2;
            epsilon_r(m) = x(1) - x(2)/r(m)^2 - 3*(1-v1^2)/8/E1*rho1*r(m)^2*ohmega^2;
            epsilon_t(m) = x(1) + x(2)/r(m)^2 - (1-v1^2)/8/E1*rho1*r(m)^2*ohmega^2;
            sigma_r(m) = E1/(1-v1^2)*(epsilon_r(m) + v1*epsilon_t(m));
            sigma_t(m) = E1*epsilon_t(m) + v1*sigma_r(m);
        elseif r(m) <= rmo
            u(m) = x(3)*r(m) + x(4)/r(m) - (1-v2^2)/8/E2*rho2*r(m)^3*ohmega^2;
            epsilon_r(m) = x(3) - x(4)/r(m)^2 - 3*(1-v2^2)/8/E2*rho2*r(m)^2*ohmega^2;
            epsilon_t(m) = x(3) + x(4)/r(m)^2 - (1-v2^2)/8/E2*rho2*r(m)^2*ohmega^2;
            sigma_r(m) = E2/(1-v2^2)*(epsilon_r(m) + v2*epsilon_t(m));
            sigma_t(m) = E2*epsilon_t(m) + v2*sigma_r(m);

        else
```

```
            u(m) = x(5)*r(m) + x(6)/r(m) - (1-v3^2)/8/E3*rho3*r(m)^3*ohmega^2;
            epsilon_r(m) = x(5) - x(6)/r(m)^2 - 3*(1-v3^2)/8/E3*rho3*r(m)^2*ohmega^2;
            epsilon_t(m) = x(5) + x(6)/r(m)^2 - (1-v3^2)/8/E3*rho3*r(m)^2*ohmega^2;
            sigma_r(m) = E3/(1-v3^2)*(epsilon_r(m) + v3*epsilon_t(m));
            sigma_t(m) = E3*epsilon_t(m) + v3*sigma_r(m);
        end
        sigma_tresca(m)                =                max([abs(sigma_t(m)                -
sigma_r(m)),abs(sigma_r(m)),abs(sigma_t(m))]);
        sigma_von_mises(m) = sqrt(sigma_r(m)^2 - sigma_t(m)*sigma_r(m) + sigma_t(m)^2);
    end


for n = 1:Steps
    if r(n) <= rfeo
        sigma_0(n) = sigma_y1/FS;
    elseif r(n) <= rmo
        sigma_0(n) = sigma_y2/FS;
    else
      sigma_0(n) = sigma_y3/FS;
    end
    sigma_0_a(n) = sigma_y3/FS;
end

toc;

figure
plot(r*1e3,sigma_r/1e6,'k')
legend('\sigma_r')
ylabel('\sigma_r (MPa)')
xlabel('Radius r (mm)')
grid on

figure
plot(r*1e3,sigma_t/1e6,'k')
legend('\sigma_t')
ylabel('\sigma_t (MPa)')
xlabel('Radius r (mm)')
grid on

figure
plot(r*1e3,sigma_von_mises/1e6,'k')
hold on
plot(r*1e3,sigma_0/1e6,'-.k','linewidth',2)
legend('\sigma_v_o_n_m_i_s_e_s','\sigma_0')
ylabel('\sigma_v_o_n_m_i_s_e_s (MPa)')
xlabel('Radius r (mm)')
grid on
```

APPENDIX II: Matlab code that plots radial, tangential and von Mises stress in SPM

```
%RADIAL AND TANGENTIAL STRESS CALCULATION FOR SURFACE PERMANENT MAGNET
%All values are given in SI units
%lITERATURE-Mechanics of Materials 2: The mechanics of elastic and plastic
%deformation of solids and structural materials(Hearn, Edwin John)
%Created by: Devika Sasi
%Date: 28.11.2017

clear all;
close all
clc;
format long
tic;

%############CONSTANTS DEFINITION############
Steps = 300; %  Number of simulation stepss
FS = 2; % factor of safety
delta_T = 0; % temperature difference
delta_r = 100e-6; %radial interference
rpm_min=0;%Minimum rpm
rpm_max = 15000;%Maximum rpm
ohmega = rpm_max/60*2*pi;%Angular velocity
CF=1.11 % Correction Fcator
% ####################################################

%############MATERIAL DATA############

%##########Core(S350)############
sigma_yfe=350e6; %Yield strength
E_fe=210e9;%Elastic modulus
v_fe=0.3;%Poisson ratio
rho_fe=7850;%Density
alpha_fe = 12e-6; %Coefficient of tehrmal expansion

%Material_2-Permanent Magnet(NdFeB)########
sigma_ym=120e6;%annealed for optimum magnetic properties
E_m=160e9;
v_m=0.24;
rho_m=7400;
alpha_m = 8e-6; % Coef. of therm. expansion
%Material_3-Titanium alloy enclosure(Ti-6Al-4V)
sigma_ye=250e6;
E_e=115e9;
v_e=0.342;
rho_e=4471;
alpha_e = 9.5e-6; % Coef. of therm. expansion
%########################################

%############GEOMETRY(in SI units)##################

r_fei = 0e-3;
r_feo = 45.5e-3 + alpha_fe*delta_T*(45.5e-3);


r_mi = 45.5e-3+ alpha_m*delta_T*(45.5e-3);
r_mo =50.5e-3+ alpha_m*delta_T*(50.5e-3);

r_ei = 50.5e-3 -delta_r + alpha_e*delta_T*(50.5e-3);
r_eo =52.5e-3+ alpha_e*delta_T*(52.5e-3);
%########################################

%####Integration Constants################

syms a b  a1_ b1_ a2_ b2_ a3_ b3_ r_ v  rho  E  sigma_r sigma_t

u = (a * r_) + b/r_ - (1 -v^2) * (rho * r_^3 * ohmega^2)/(8*E);%Displacement Equation [REFER
EQUATION (24)]

epsr = diff(u,'r_')% Radial strain Equation 1 [REFER EQUATION (18)]
epst = u/r_% Tangential strain Equation 1 [REFER EQUATION (19)]

epsr_ = 1/E * (sigma_r - v * sigma_t);% Radial strain Equation 2 [REFER EQUATION (21)]
epst_ = 1/E * (sigma_t - v * sigma_r);% Tangential strain Equation 2 [REFER EQUATION (22)]
```

```
res1 = epsr - epsr_;
res2 = epst - epst_;

sigma_t_ = solve(res2, sigma_t)%Tangential stress

res3 = subs(res1,sigma_t,sigma_t_);

res4 = res3 == 0

sigma_r_= isolate(res4,sigma_r)%Radial Stress

%#################Stress&Displacement Equations#############################

sigma_r_feo=subs(rhs(sigma_r_),[r_,a,b,E,v,rho],[r_feo,a1_,b1_,E_fe,v_fe,rho_fe]);
sigma_r_mi=subs(rhs(sigma_r_),[r_,a,b,E,v,rho],[r_mi,a2_,b2_,E_m,v_m,rho_m]);
u_r_feo=subs(u,[r_,a,b,E,v,rho],[r_feo,a1_,b1_,E_fe,v_fe,rho_fe]);
u_r_mi= subs(u,[r_,a,b,E,v,rho],[r_mi,a2_,b2_,E_m,v_m,rho_m]);
sigma_r_mo=subs(rhs(sigma_r_),[r_,a,b,E,v,rho],[r_mo,a2_,b2_,E_m,v_m,rho_m]);
sigma_r_ei=subs(rhs(sigma_r_),[r_,a,b,E,v,rho],[r_ei,a3_,b3_,E_e,v_e,rho_e]);
u_r_mo=subs(u,[r_,a,b,E,v,rho],[r_mo,a2_,b2_,E_m,v_m,rho_m]);
u_r_ei= subs(u,[r_,a,b,E,v,rho],[r_ei,a3_,b3_,E_e,v_e,rho_e])
sigma_r_eo=subs(rhs(sigma_r_),[r_,a,b,E,v,rho],[r_eo,a3_,b3_,E_e,v_e,rho_e]);
%#########################################################################

%######################BOUNDARY CONDITIONS#################################
bound_1=b1_==0;
bound_2=sigma_r_feo==sigma_r_mi;
bound_3=r_feo+u_r_feo==r_mi+u_r_mi;
bound_4=sigma_r_mo==sigma_r_ei;
bound_5=r_mo+u_r_mo==r_ei+u_r_ei;
bound_6=sigma_r_eo==0;
%#########################################################################

%######################SOLUTION############################################
sol=solve([bound_1,bound_2,bound_3,bound_4,bound_5,bound_6],[a1_,a2_,a3_,b1_,b2_,b3_]);
a1=sol.a1_;
a2=sol.a2_;
a3=sol.a3_;
b1=sol.b1_;
b2=sol.b2_;
b3=sol.b3_;

x=double([a1 b1 a2 b2 a3 b3]')


%#########################################################################
r = linspace(r_fei+50e-6,r_eo,Steps);%Radius
u = zeros(Steps,1);%Dispalcement
epsilon_r = zeros(Steps,1);%Radial strain
epsilon_t = zeros(Steps,1);%Tangential strain
sigma_ref_max = zeros(Steps,1);%Reference stress



    for m = 1:Steps % Radius loop
        if r(m) <= r_feo
            u(m) = x(1)*r(m) + x(2)/r(m) - (1-v_fe^2)/8/E_fe*rho_fe*r(m)^3*ohmega^2;
            epsilon_r(m) = x(1) - x(2)/r(m)^2 - 3*(1-v_fe^2)/8/E_fe*rho_fe*r(m)^2*ohmega^2;
            epsilon_t(m) = x(1) + x(2)/r(m)^2 - (1-v_fe^2)/8/E_fe*rho_fe*r(m)^2*ohmega^2;
            sigma_r(m) = E_fe/(1-v_fe^2)*(epsilon_r(m) + v_fe*epsilon_t(m));
            sigma_t(m) = E_fe*epsilon_t(m) + v_fe*sigma_r(m);
        elseif r(m) <= r_mo
            u(m) = x(3)*r(m) + x(4)/r(m) - (1-v_m^2)/8/E_m*rho_m*r(m)^3*ohmega^2;
            epsilon_r(m) = x(3) - x(4)/r(m)^2 - 3*(1-v_m^2)/8/E_m*rho_m*r(m)^2*ohmega^2;
            epsilon_t(m) = x(3) + x(4)/r(m)^2 - (1-v_m^2)/8/E_m*rho_m*r(m)^2*ohmega^2;
            sigma_r(m) = E_m/(1-v_m^2)*(epsilon_r(m) + v_m*epsilon_t(m));
            sigma_t(m) = E_m*epsilon_t(m) + v_m*sigma_r(m);

        else
            u(m) = x(5)*r(m) + x(6)/r(m) - (1-v_e^2)/8/E_e*rho_e*r(m)^3*ohmega^2;
            epsilon_r(m) = x(5) - x(6)/r(m)^2 - 3*(1-v_e^2)/8/E_e*rho_e*r(m)^2*ohmega^2;
            epsilon_t(m) = x(5) + x(6)/r(m)^2 - (1-v_e^2)/8/E_e*rho_e*r(m)^2*ohmega^2;
            sigma_r(m) = E_e/(1-v_e^2)*(epsilon_r(m) + v_e*epsilon_t(m));
            sigma_t(m) = E_e*epsilon_t(m) + v_e*sigma_r(m);
```

```
        end
        sigma_tresca(m)                =                max([abs(sigma_t(m)                -
sigma_r(m)),abs(sigma_r(m)),abs(sigma_t(m))]);
        sigma_von_mises(m) = sqrt(sigma_r(m)^2 - sigma_t(m)*sigma_r(m) + sigma_t(m)^2);
    end

toc

for n = 1:Steps
    if r(n) <= r_feo
        sigma_ref(n) = sigma_yfe/FS;
    elseif r(n) <= r_mo
        sigma_ref(n) = sigma_ym/FS;
    else
      sigma_ref(n) = sigma_ye/FS;
    end
    sigma_0_a(n) = sigma_ye/FS;
end



figure
plot(r*1e3,sigma_r/1e6,'k')
legend('\sigma_r')
ylabel('\sigma_r (MPa)')
xlabel('Radius r (mm)')
grid on

figure
plot(r*1e3,sigma_t/1e6,'k')
legend('\sigma_t')
ylabel('\sigma_t (MPa)')
xlabel('Radius r (mm)')
grid on

figure
plot(r*1e3,sigma_von_mises/1e6,'k')
hold on
plot(r*1e3,sigma_ref/1e6,'-.k','linewidth',2)
legend('\sigma_v_o_n_m_i_s_e_s','\sigma_ref')
ylabel('\sigma_v_o_n_m_i_s_e_s (MPa)')
xlabel('Radius r (mm)')
grid on

format bank

Stress_above_Permannet_magnet=double((max(sigma_t)))*1e-6 %in MPa
Stress_above_Permannet_magnet_Corrected=CF*(double((max(sigma_t))))*1e-6 %in MPa
```

APPENDIX III : Matlab code that calculates maximum tangential stress in IPM

```
%Literature-Fixation of Buried and Surface-Mounted Magnets in High-Speed
%Permanent-Magnet Synchronous Machines
%The shaft and iron core is assumed as a single entity in ths approach
%An equivalent ring is proposed to replace the magnet and iron bridge at
%the outer periphery of magnet based on literature
%6 pole magnet is considered
%Created by: Devika Sasi
%Date: 28.11.2017

clear all;
close all
clc;
tic;
format short
%###################General parameters#############
delta_T=0;%temperature difference assume to be constant between rotor structure and ambient
temperature
rpmmin=0;%Minimum rpm
rpmmax = 30000;%Maximum rpm
ohmega = rpmmax/60*2*pi;%Angular velocity
CF=1.88

%###########Material Data(in SI Units)###############
%Material Data
%#############Iron core (S350)####################
rho_fe=7850;                  %Density
E_fe=210e9;                   %Elastic Modulus
v_fe=0.3;                     %Poissons ratio
alpha_fe=12e-6;               %Coefficient of thermal expansion
sigma_yfe=350e6;              %yield strength
%#############Permanet magnet(NdFeB)################
rho_m=7400;
E_m=160e9;
v_m=0.24;
alpha_m=8e-6;
sigma_ym=120e6;
%#############GEOMETRY(in SI units)#################

r_fei = 0e-3; %Inner radius of iron core
r_feo = (94/2)*1e-3% Outer radius of iron core

l_m=20e-3;% length of a single magnet pole
b_m=4e-3;% breadth of a single magnet pole

h_eq=2e-3;%Height of the proposed equivalent ring from outermost radius
beta=pi/4;%Pole anle of a single magnetic pole

%#####Centroid Calculation#################
 r_eqo=r_feo %equivalent ring outside radius [REFER EQUATION(43)]
  r_eqi=r_feo-h_eq %equivalent ring inside radius [REFER EQUATION(43)]


  R1=2*r_eqo*sin(beta/2)/(3*(beta/2)) % [REFER EQUATION (44)]
  A1=(beta/2)*(r_eqo)^2 % [REFER EQUATION (45)]
  R2=2*(r_eqi-b_m)*sin(beta/2)/(3*(beta/2)) % [REFER EQUATION (44)]
  A2=(beta/2)*(r_eqi-b_m)^2 % [REFER EQUATION (45)]
  R3=r_eqi-(b_m/2) % [REFER EQUATION (44)]
  A3=b_m*l_m % [REFER EQUATION (45)]

  r_cm=r_eqi-(b_m/2)%Centroid of magnet [REFER EQUATION (46)]
  r_cfe=(R1*A1-(R2*A2)-(R3*A3))/(A1-A2-A3)%Centroid of Iron bridge[REFER EQUATION (46)]

  %##########################################

  %#############Equivalent ring calculation#######

% r_ceq=(r_eqi+r_eqo)/2 )%Alternate equation for centroid of equivalent ring
 R4=2*r_eqi*sin(beta/2)/(3*(beta/2)) [REFER EQUATION (44)]
  A4=(beta/2)*(r_eqi)^2 [REFER EQUATION (45)]
r_ceq=(R1*A1-R4*A4)/(A1-A4)%Centroid of equivalent ring [REFER EQUATION (46)]
   r_ceq=r_feo*sin(beta/2)/(beta/2)%Alternate equation for centroid of equivalent ring
  A_m=b_m*l_m; %Area of magnet [REFER EQUATION (45)]
```

```
  A_fe=A1-A2-A3;%Total area of iron bridge above and on sides of magnet [REFER EQUATION (45)
]
  A_eq=beta/2*(r_eqo^2-r_eqi^2)% area of equivalent ring [REFER EQUATION (45)]
  rho_eq=(r_cm*rho_m*A_m+r_cfe*rho_fe*A_fe)/(r_ceq*A_eq)%density of equivalent ring [REFER
EQUATION (47)]


%################################################

%############Tangential stress calculation#########
sigma_teq=r_ceq^2*ohmega^2*rho_eq*1e-6 %[REFER EQUATION (47)]

sigma_teq_corrected=CF* r_ceq^2*ohmega^2*rho_eq*1e-6
```

APPENDIX IV: Matlab code that calculates maximum tangential stress in VPM

```
% Literature-Calculation of the Maximum Mechanical Stress on the Rotor of
%Interior Permanent-Magnet Synchronous Motors
%Created by: Devika Sasi
%Date: 28.11.2017


clear all;
close all
clc;
tic;
%##################General parameters#############
%delta_T=100;%temperature difference assume to be constant between rotor structure and ambient
temperature
rpmmin=0;%Minimum rpm
rpmmax = 15000;%Maximum rpm
ohmega = rpmmax/60*2*pi;%Angular velocity
SF=3.07%stress concentration factor

%##########Material Data(in SI Units)##############
%Material Data
%############Iron core (S350)###################
rho_fe=7850;                  %Density
E_fe=210e9;                   %Elastic Modulus
v_fe=0.3;                     %Poissons ratio
alpha_fe=12e-6;               %Coefficient of thermal expansion
sigma_yfe=350e6;              %yield strength
%#############Permanet magnet(NdFeB)###############
rho_m=7400;
E_m=160e9;
v_m=0.24;
alpha_m=8e-6;
sigma_ym=120e6;
%############GEOMETRY(in SI units)#################

r_fei = 0e-3; %Inner radius of iron core
r_feo =(84/2)*1e-3% Outer radius of iron core
l_m=16e-3;% length of a single magnet pole
b_m=3e-3;% breadth of a single magnet pole
h_eq=2e-3;%Height of the proposed equivalent ring from outermost radius

alpha=60/180*3.14; %pole shoe angle
theta=150/180*3.14;%Angle between a pair of V magnets

r_eqi=r_feo-h_eq %Inner radius of equivalent ring [REFER EQUATION (48)]
r_eqo=r_feo%Outer radius of equivalent ring [REFER EQUATION (48)]
%#############EQUATIONS############################

r_m=r_eqi*cos(alpha/2)-(r_eqi*sin(alpha/2)*cot(theta/2)+b_m/(2*sin(alpha/2))-
(b_m/2*cot(theta/2)+b_m+l_m/2)*cos(theta/2)) %[REFER EQUATION (49)]
A_m=2*(l_m*b_m);%Total area of magnet assuming both magnets to be of equal area [REFER
EQUATION (58)]

x_fe_1=2/3*(r_eqo^3-r_eqi^3)*sin(alpha); % Centroid of region 1 [REFER EQUATION (51)]
x_fe_2=2/3*r_eqi^3*(sin(alpha/2)-cos(alpha/2).^3*tan(alpha/2)); % Centroid of region 2 [REFER
EQUATION (55)]
x_fe_3=r_eqi^3*(sin(alpha/2).^2*cos(alpha/2)*cot(theta/2)-
1/3*sin(alpha/2).^3*cot(theta/2).^2) % Centroid of region 3[REFER EQUATION (53)]
A_fe_1=alpha*(r_eqo^2-r_eqi^2); % Area of region 1 [REFER EQUATION (54)]
A_fe_2=1/2*r_eqi^2*(alpha-sin(alpha)); % Area of region 2 [REFER EQUATION (55)]
A_fe_3=r_eqi^2*sin(alpha/2).^2*cot(theta/2); % Area of region 3[REFER EQUATION (56)]

A_fe=A_fe_1+A_fe_2+A_fe_3; % Tota area of iron bridge [REFER EQUATION (59)]
r_fe=(x_fe_1+x_fe_2+x_fe_3)/(A_fe_1+A_fe_2+A_fe_3); %[REFER EQUATION  (50)]

r_o=(r_eqo+r_eqi)/2; %[REFER EQUATION (61)]
A_eq=A_fe_1; %[REFER EQUATION (60)]
rho_eq=(r_m*rho_m*A_m+r_fe*rho_fe*A_fe)*((1-cos(theta))/2)/(r_o*A_eq); %[REFER EQUATION (57)
]
%#######################################################

%###############STRESS CALCULATION##################
sigma_t=r_o^2*ohmega^2*rho_eq*1e-6 %MPa %[REFER EQUATION (62)]
sigma_peak=SF*sigma_t % [REFER EQUATION (63)
```